Precambrian Research 432 (2026) 107968

Contents lists available at ScienceDirect

Precambrian Research

journal homepage: www.elsevier.com/locate/precamres

Research Paper

Resolving the *syn*-genetic mineralization age of a metamorphosed Archean VHMS deposit using multiple geochronological approaches

Cendi D.P. Dana [a,*], Steven P. Hollis [a], Lorenzo Tavazzani [b], Cyril Chelle-Michou [b], Stijn Glorie [c], Yusuke Kuwahara [d,e,1], Kazuhide Mimura [d,2], Moei Yano [d,e], Junichiro Ohta [e,d], David Selby [f], Yasuhiro Kato [e,d], Vanessa Pashley [g], Megan James [h], Darryl Podmore [h]

[a] School of GeoSciences, Grant Institute, The University of Edinburgh, Edinburgh EH9 3FE, United Kingdom
[b] Department of Earth and Planetary Sciences, ETH Zurich, Zurich 8092, Switzerland
[c] Department of Earth Sciences, University of Adelaide, South Australia 5005, Australia
[d] Ocean Resources Research Center for Next Generation, Chiba Institute of Technology, Chiba 275-0016, Japan
[e] Department of Systems Innovation, School of Engineering, The University of Tokyo, Tokyo 113-8656, Japan
[f] Department of Earth Sciences, University of Durham, Durham DH1 3LE, United Kingdom
[g] Geochronology and Tracers Facility, British Geological Survey, Nottingham NG12 5GG, United Kingdom
[h] Black Raven Mining, PO Box 261, North Perth, Western Australia 6872, Australia

ARTICLE INFO

Keywords:
Geochronology
VMS
Yilgarn Craton
U–Pb
Re–Os
Lu–Hf
Pb isotopes

ABSTRACT

Accurately determining the timing of mineralization is essential for exploring *syn*-genetic stratiform mineral systems, such as volcanic-hosted massive sulfide (VHMS) deposits. This study integrates multiple geochronological techniques to constrain both the age of *syn*-genetic mineralization and subsequent overprinting magmatic, metamorphic and deformation events at the King VHMS deposit, Western Australia. The timing of *syn*-genetic mineralization is collectively constrained by consistent ages from U–Pb zircon geochronology of host felsic volcanic rocks (2725 ± 10 Ma), a Re–Os pyrite isochron (2730 ± 26 Ma), and Pb–Pb galena model ages (ca. 2714–2718 Ma). Pyrrhotite, formed via metamorphic desulfidation of pyrite, records a younger Re–Os age of 2652 ± 32 Ma, overlapping with the timing of prograde metamorphism dated by *in situ* Lu–Hf garnet analysis at 2680 ± 28 Ma. A Re–Os age from massive sulfide ore (2664 ± 23 Ma), reflecting a mixture of pyrite and pyrrhotite, produces a geologically meaningless average due to metamorphic re-equilibration, highlighting limitations of bulk Re–Os dating in high-grade metamorphosed systems. Quartz monzonite intrusions that crosscut the deposit and are associated with the regional M2 metamorphism yielded weighted mean U–Pb zircon ages of ca. 2676–2665 Ma, and are associated with minor molybdenite mineralization (Re–Os ages ca. 2650–2655 Ma). Collectively, these results confirm that the King Zn deposit represents the first phase of VHMS mineralization during the formation of the Kalgoorlie-Kurnalpi Rift (KKR), and significantly predates other VHMS deposits of the Eastern Goldfields. This study also demonstrates that the Re–Os isotopic signature of *syn*-genetic pyrite can be retained through amphibolite-facies metamorphism, providing a new opportunity to directly date VHMS deposits affected by high-grade metamorphism in Archean cratons globally. In contrast, Re–Os ages of pyrrhotite record prograde metamorphism, offering a potential tool for constraining metal remobilization events.

1. Introduction

Determining the age of mineral deposits and their host rock sequences is fundamental for exploration, as it not only establishes the temporal framework of prospective geological formations but also elucidates the regional geodynamic events (e.g., tectonism, metamorphism, magmatism and/or volcanism) responsible for ore formation (e.g., Hollis et al., 2015; Chiaradia, 2023; Dana et al., 2024). This is particularly crucial for *syn*-genetic stratiform mineral systems, such as volcanic-hosted massive sulfide (VHMS) deposits. These deposits are

* Corresponding author.
E-mail address: c.d.p.dana@sms.ed.ac.uk (C.D.P. Dana).
[1] Current affiliation: School of Biological and Environmental Sciences, Kwansei Gakuin University, Hyogo 669-1330, Japan.
[2] Geological Survey of Japan, National Institute of Advanced Industrial Science and Technology, Ibaraki 305-8567, Japan.

https://doi.org/10.1016/j.precamres.2025.107968
Received 22 July 2025; Received in revised form 23 October 2025; Accepted 10 November 2025

typically clustered within volcanic belts along geologically favorable stratigraphic horizons and are intimately linked to episodes of regional extension and magmatism (e.g., Goodfellow and McCutcheon, 2003; Barrote et al., 2020a; Kelly et al., 2024). However, in Archean cratons these deposits are often affected by multiple post-ore metamorphic and deformation events, which can obscure the primary isotopic signatures of the original deposit (e.g., Araujo and Scott, 1996; Burton et al., 2000; González-Jiménez et al., 2012) and lead to local metal remobilization (e.g., Plimer, 1987; Marshall et al., 1998; Tomkins, 2007). In some instances, VHMS deposits can also be overprinted by younger hydrothermal-magmatic events associated with orogenic Au mineralization (e.g., Mt. Gibson: Yeats and Groves, 1998; Kelan: Xu et al., 2011; Yushui: Chen et al., 2023), hampering efforts to constrain the age of the early *syn*-genetic mineralization.

In the Archean Yilgarn Craton of Western Australia (Fig. 1), the timing of VHMS mineralization is well constrained in the northwest Youanmi Terrane (Hollis et al. 2015), but remains poorly constrained across several understudied greenstone belts, particularly in the eastern Youanmi Terrane (e.g., Gum Creek, Copper Bore), Southwest Terrane (e.g., Wheatley) and most parts of the Eastern Goldfields Superterrane (EGST). Although several studies have attempted to date VHMS deposits across the Yilgarn Craton, robust geochronological constraints have so far only been obtained from U–Pb zircon ages of the felsic host rocks (e.g., Hayman et al. 2015; Hollis et al. 2015, 2017a), and limited Re–Os ages of nodular pyrite and black shale at Nimbus (e.g., Barrote et al., 2021), though the latter often have considerable uncertainty. Attempts to apply ^{40}Ar–^{39}Ar geochronology on sericitised plagioclase laths and U–Pb monazite dating at Nimbus yielded significantly younger dates, associated with post-ore granitoid emplacement (Barrote et al., 2020b). While Pb–Pb galena model ages are generally consistent with host rock ages for VHMS deposits, significant discrepancies exist between model ages and footwall rocks of ca. 40–25 Myr depending on the model used (Maltese and Mezger, 2020; Zametzer et al., 2022, 2023) and analytical uncertainties associated with Pb isotope analysis.

In this study, we employ multiple geochronological approaches (U–Pb zircon and titanite; Lu–Hf garnet; Re–Os sulfide and molybdenite; Pb–Pb galena) to constrain the *syn*-genetic mineralization age of the King VHMS deposit. The combination of these chronometers also allows us to understand the timing of subsequent events related to late granite emplacement and associated molybdenite mineralization, prograde amphibolite-facies metamorphism and late Proterozoic deformation. The findings are significant for constraining the age of metamorphosed VHMS deposits globally, and aiding regional exploration targeting across the Yilgarn Craton.

2. Geological background

2.1. Tectono-magmatic evolution of the Yilgarn Craton

The Yilgarn Craton is composed of distinct tectono-metamorphic terranes, each with unique deformation intensities and metamorphic, stratigraphic, and magmatic histories. From west to east, these terranes

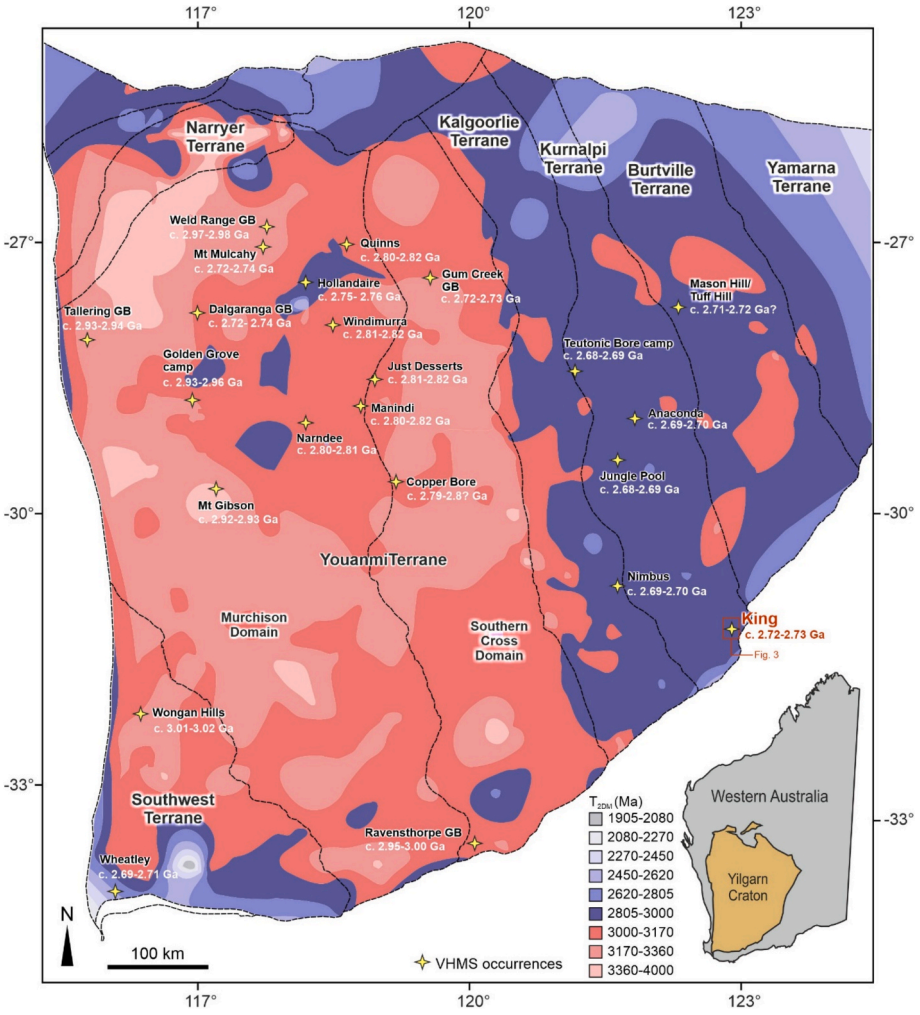

Fig. 1. Yilgarn regional Lu–Hf_{zircon} map contoured for T_{2DM} ages and distribution of major VHMS deposits/occurrences (modified after Smithies et al., 2023). Location of the King deposit and nearby prospects is highlighted with red square.

include the Narryer, Southwest, Youanmi, Kalgoorlie, Kurnalpi, Burtville and Yamarna terranes. The Paleo-Mesoarchean West Yilgarn (i.e., Narryer, Southwest, Youanmi) is separated from the Neoarchean Eastern Goldfields Superterrane (EGST) by the Ida Fault Zone. The geological characteristics of each terrane have been thoroughly documented by previous studies (e.g., Cassidy et al., 2006, Goscombe et al., 2019). The stratigraphic and deformation history of the Yilgarn Craton (Fig. 2) can be divided into several key periods, which are outlined below.

2.1.1. *West Yilgarn Craton*

The Narryer and Southwest terranes are primarily composed of granite and granitic gneiss, with minor inliers of supracrustal greenstone. In the Narryer Terrane, the oldest units are the ~ 3.7 Ga Manfred Complex and Meeberrie Gneiss, which were subsequently intruded by ~ 3.3 Ga felsic magmas (Wyche et al., 2014). In the Southwest Terrane, the oldest supracrustal successions (ca. 3.2–3.0 Ga) are found in the Chittering, Jimperding, and Balingup metamorphic belts. These were later intruded by granitic and pegmatite bodies dated between ~ 2.75 and 2.62 Ga (Mole et al., 2012).

In the Youanmi Terrane, early supracrustal sequences formed between ~ 3.0 and 2.9 Ga, marking the earliest phase of crustal extension and volcanism (e.g., Twin Peaks, Tallering, Lake Johnston greenstone belts; Goscombe et al., 2019). Notably, the greenstone sequences from this period often host volcanogenic massive sulfide (VHMS) mineralization (e.g., Golden Grove, Mt. Gibson, and Weld Range; Yeats & Groves, 1998; Sharpe & Gemmell, 2002; Guilliamse, 2014). These older supracrustal units are unconformably overlain by the Norrie Group (ca. 2825–2805 Ma), dominated by mafic–ultramafic rocks and their intrusive equivalents (Ivanic et al., 2010; van Kranendonk et al., 2013). This major mantle melting event, possibly plume-driven, may have contributed to partial breakup of the proto-Yilgarn Craton driving east–west extension (Ivanic et al., 2010; Czarnota et al., 2010; Mole et al., 2015). Overlying felsic volcanic rocks of the Kantie Murdana Volcanics Member and Yaloginda Formation host VHMS mineralization at Austin-Quinns, Just Desserts and Yuinmery (Ivanic et al. 2010; Hassan 2014; Duuring et al. 2016).

The Norrie Group is disconformably overlain by the Polelle Group (ca. 2800–2730 Ma), which includes older mafic–ultramafic sequences (e.g., 2800–2760 Ma Meekatharra Formation) and younger intermediate-felsic volcanic rocks (e.g., 2760–2740 Ma Greensleeves Formation; van Kranendonk et al., 2013). The latter formation hosts VHMS mineralization at Hollandiare, Jillewarra, Mt Mulchay and Dalgaranga (Hayman et al. 2015; Hollis et al. 2017b). Subsequently, the Polelle Group was unconformably overlain by the Glen Group (ca.

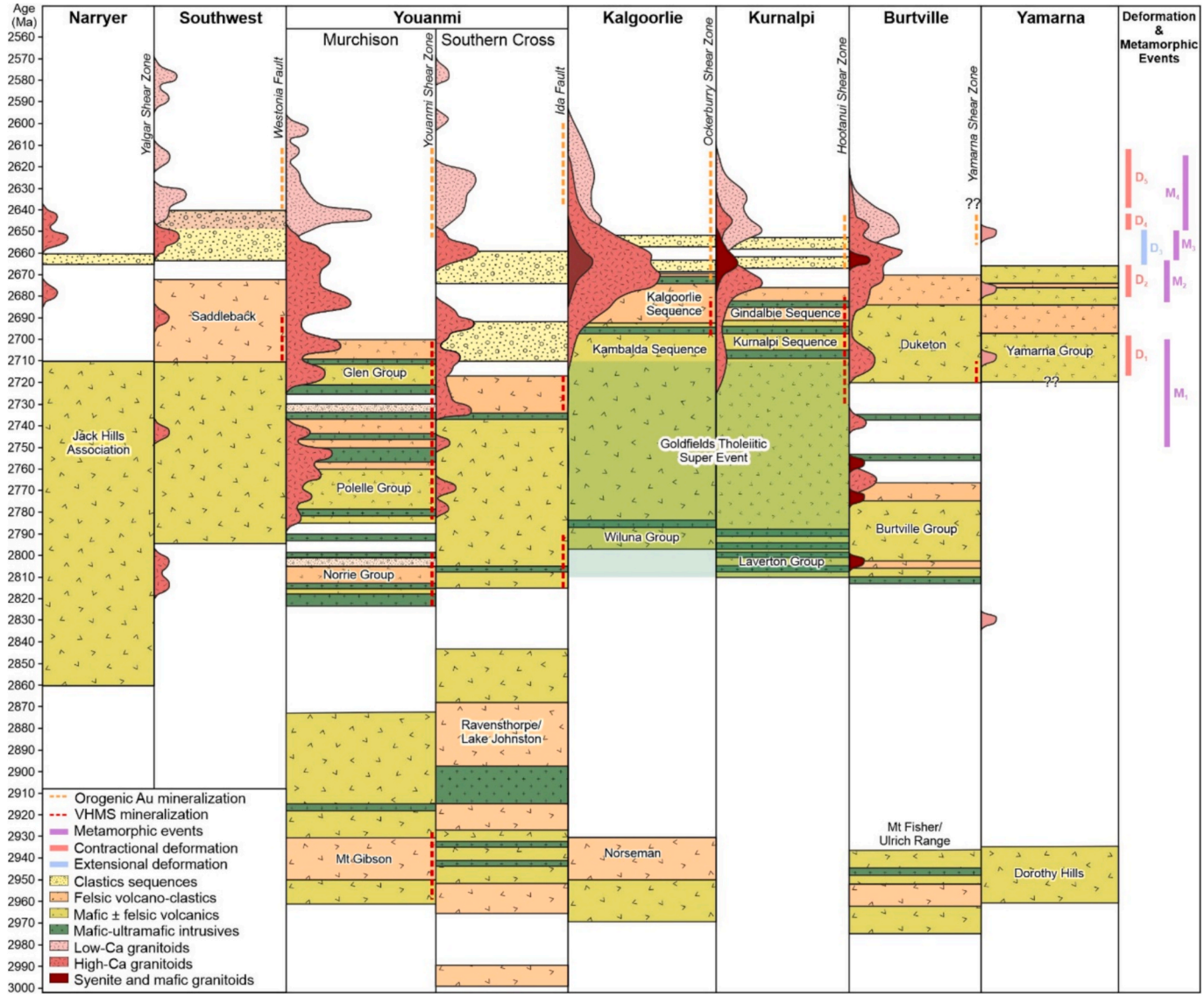

Fig. 2. Regional correlation of stratigraphy, deformation and timing of mineralization across the Archean Yilgarn Craton (modified after Goscombe et al., 2019).

2735–2700 Ma), which consists of mostly clastic sedimentary rocks (i.e., Ryansville Formation) and komatiitic basalts with minor rhyolite (i.e., Wattagee Formation; Ivanic et al., 2010; Wyche et al., 2014). The Glen Group is broadly equivalent to the ca. 2725–2720 Ma Gum Creek greenstone belt in the Southern Cross Domain, which is notable for its abundant clastic sediments, including graphitic shale spatially associated with VHMS mineralization at the Altair, The Cup, and Bevan deposits (e.g., Bodorkos et al., 2006; Hollis et al. 2015). The ca. 2734–2730 Ma Marda-Diemals greenstone belts in the Southern Cross Domain may also broadly correlate to the Glen Group (Chen et al., 2003; Morris et al., 2007).

2.1.2. Eastern Goldfields Superterrane (EGST)

The oldest supracrustal record in the Kalgoorlie and Kurnalpi Terranes is preserved as poorly exposed fragments of ca. 2.96–2.93 Ga granitic gneiss basement (e.g., Nelson, 1995; Mole et al., 2015). This basement is overlain by a ~ 2.81–2.71 Ga tholeiite-dominated volcanic succession termed the Goldfields Tholeiitic Super Event (Hayman et al., 2015; Austin et al., 2022). These older sequences are then unconformably overlain by ~ 2.71–2.66 Ga greenstone successions which are widely exposed across the Kalgoorlie and Kurnalpi terranes. In the Kalgoorlie Terrane, this includes the ultramafic–mafic Kambalda Sequence (ca. 2710–2692 Ma; Beresford et al., 2005; Austin et al., 2022), which is overlain by the felsic volcanic/volcaniclastic Kalgoorlie Sequence (ca. 2690–2660 Ma; Krapež and Hand, 2008) that includes the TTG-like Black Flag Group. In the Kurnalpi Terrane, the older greenstone succession is represented by the Kurnalpi Sequence (ca. 2720–2700 Ma; Kositcin et al., 2008; Austin et al., 2022), which is overlain by bimodal volcanic rocks across the Gindalbie Sequence (ca. 2660–2650 Ma; Kositcin et al., 2008). To the east, these sequences are equivalent to the Yamarna Group (ca. 2720–2670 Ma; Pawley et al., 2012; Goscombe et al., 2019). All of these successions were later intruded by granites associated with the widespread ~ 2.74–2.65 Ga High-Ca and ~ 2.66–2.63 Ga Low-Ca granite bloom (e.g., Cassidy and Champion, 2004; Czarnota et al., 2010; Goscombe et al., 2019). Previous studies suggested that the formation of these greenstone sequences correspond to a prolonged period of ENE-directed extension (D1) between 2720 and 2690 Ma alongside bimodal volcanism and extensive high-Ca granite intrusions (e.g., Groenewald et al., 2006; Goscombe et al., 2019).

In the EGST significant VHMS mineralization is largely confined to the Kalgoorlie-Kurnalpi Rift (KKR) and dates to approximately 2705–2680 Ma (Hollis et al., 2015; 2017b). Three main deposits have been mined from the ca. 2690 Ma Gindalbie volcanic rocks at the Teutonic Bore camp (i.e., Teutonic Bore, Jaguar, and Bentley; Belford, 2010; Barrote et al., 2020a). Smaller VHMS occurrences have also been recognized from ca. 2700 Ma felsic tuffs of the Kurnalpi Sequence (e.g., Anaconda), and the King Zn deposit at Erayinia in southern Kurnalpi (Hollis et al., 2019a,b). Additional Ag-Zn-(Au) mineralization is found at Nimbus (ca. 2703 Ma), located on the margin of the Kalgoorlie Terrane (Hollis et al., 2017a; Barrote et al., 2020b).

2.2. Metamorphic history of the Yilgarn Craton

The metamorphic history of the Yilgarn Craton can be broadly subdivided into five stages based on overprinting relationships among structural, magmatic, and metamorphic mineral growth events described above, as well as distinct metamorphic responses in different tectono-stratigraphic settings. The records of an initial metamorphic event are very limited, and the P-T conditions are generally unknown due to extensive reworking and metamorphism during the Neoarchean (Goscombe et al., 2019). The oldest (ca. 3300–3180 Ma) metamorphic records are preserved in the Narryer and Southwest terranes in the form of metapelite granulite (Nieuwland and Compston, 1981; Kinny and Nutman, 1996; Wilde and Spaggiari, 2007).

The early Neoarchean metamorphism (M0) is characterized by low-pressure/high-temperature (low-P/high-T) upper amphibolite to granulite facies conditions limited to ca. ~ 2730–2690 Ma and primarily occurring within magmatic arcs in the Kurnalpi and Burtville terranes, such as within the Gindalbie and Duketon volcanic rocks (e.g., Barley et al., 2006; Cassidy et al., 2006; Goscombe et al., 2019). The second phase (M1) involved high-P/moderate-T metamorphism (Barrovian series), and is linked to accretion and partial burial of magmatic arc margins during ca. 2748–2706 Ma (e.g., Cassidy et al., 2006; Goscombe et al., 2009; Champion and Cassidy, 2010; Goscombe et al., 2019). Following this event, regional-contact metamorphism (M2, low-P/moderate-T) associated with high-Ca granite emplacement and contraction (D2) occurred during ca. 2685–2665 Ma (e.g., Cassidy et al., 2006; Goscombe et al., 2009; Czarnota et al., 2010; Goscombe et al., 2019). Extension-related metamorphism (M3) overprints M2 and is characterized by low-P/moderate-T (Buchan series) metamorphism associated with lithospheric extension during ca. 2665–2650 Ma, localized in post-volcanic clastic basins or along D3 shear zones (e.g., Goscombe et al., 2009; Czarnota et al., 2010; Goscombe et al., 2019). The final stage of regional low-P/high-T metamorphism (M4) was driven by renewed contraction (i.e., D4–D5) and the arrival of a diffusion-delayed thermal anomaly, likely triggered by lower-crust and mantle lithosphere delamination during ca. 2650–2610 Ma (e.g., Champion and Sheraton, 1997; Champion and Cassidy, 2007; Goscombe et al., 2019). Following this peak metamorphic activity, waning thermal flux continued resetting isotopic systems between 2610–2545 Ma, with the cratonization process concluded before 2410 Ma (Goscombe et al., 2019 and references therein).

2.3. Geology of the King deposit and surrounding areas

The geology of the King deposit (2.15 Mt at 3.5 % Zn, 0.3 % Pb, 15 g/t Ag, 0.2 g/t Au) has been well characterized by several previous studies (Hollis et al., 2019b; Kelly et al., 2024; Dana et al., 2025) which are summarized as follows. Regionally, the King deposit is located in the Erayinia region at the southern part of the Kurnalpi Terrane where two major faults (i.e., Claypan and Roe Hills faults) separate the region into three domains: (i) Edjudina; (ii) Murrin; and (iii) Menangina (Fig. 3). The stratigraphy of the King deposit belongs to the Edjudina domain, predominantly composed of mafic-felsic metavolcanic complexes overlain by metasedimentary sequences including chert and banded iron formation (Swager 1995; 1997).

Currently, geochronological data for this region is very limited. The most recent U–Pb zircon ages (SHRIMP) are from an intermediate felsic unit (2685 ± 8 Ma) in the Erayinia NW area which is part of Murrin domain, and is crosscut by a monzonite intrusion (2686 ± 11 Ma; Hollis et al., 2019a). Previous studies also reported U–Pb ages (SHRIMP) of a metasiltstone unit from the Karonie mine (2703 ± 5 Ma; Wingate and Bodorkos, 2007a) and a rhyolitic volcaniclastic rock from the Erayinia NW (2680 ± 5 Ma; Wingate and Bodorkos, 2007b), which are also part of Murrin domain. On the other hand, U–Pb zircon ages (SHRIMP) from the Edjudina domain range from 2708 ± 6 Ma (i.e., fragmental metadacite porphyry in a felsic sequence ~ 100 km north of King; Nelson, 1995) to 2680 ± 4 Ma (i.e., granite gneiss at Coonana Hill 30 km NE of King; Wingate et al. 2016).

At the deposit scale, the King deposit is hosted within an overturned, east-dipping, volcanic-dominated stratigraphy that was metamorphosed to amphibolite facies. The footwall sequences consist of deeper mafic and overlying intermediate-felsic units. The footwall mafic units comprise mafic-derived metasedimentary rocks (i.e., biotite-muscovite schist; Fig. 4i,j), overlain by tholeiitic mafic metavolcanics (i.e., garnet amphibolite; Fig. 4k,l). The footwall intermediate-felsic units consist of calc-alkaline lower- and upper-felsic metavolcanics (i.e., chlorite-muscovite-quartz schist), which are separated by a narrow, intensely Mg-altered felsic metavolcanic zone (i.e., muscovite-chlorite schist). Overlying the footwall felsic units are the hanging-wall units, which include thin metaexhalite horizons (i.e., strongly banded magnetite-

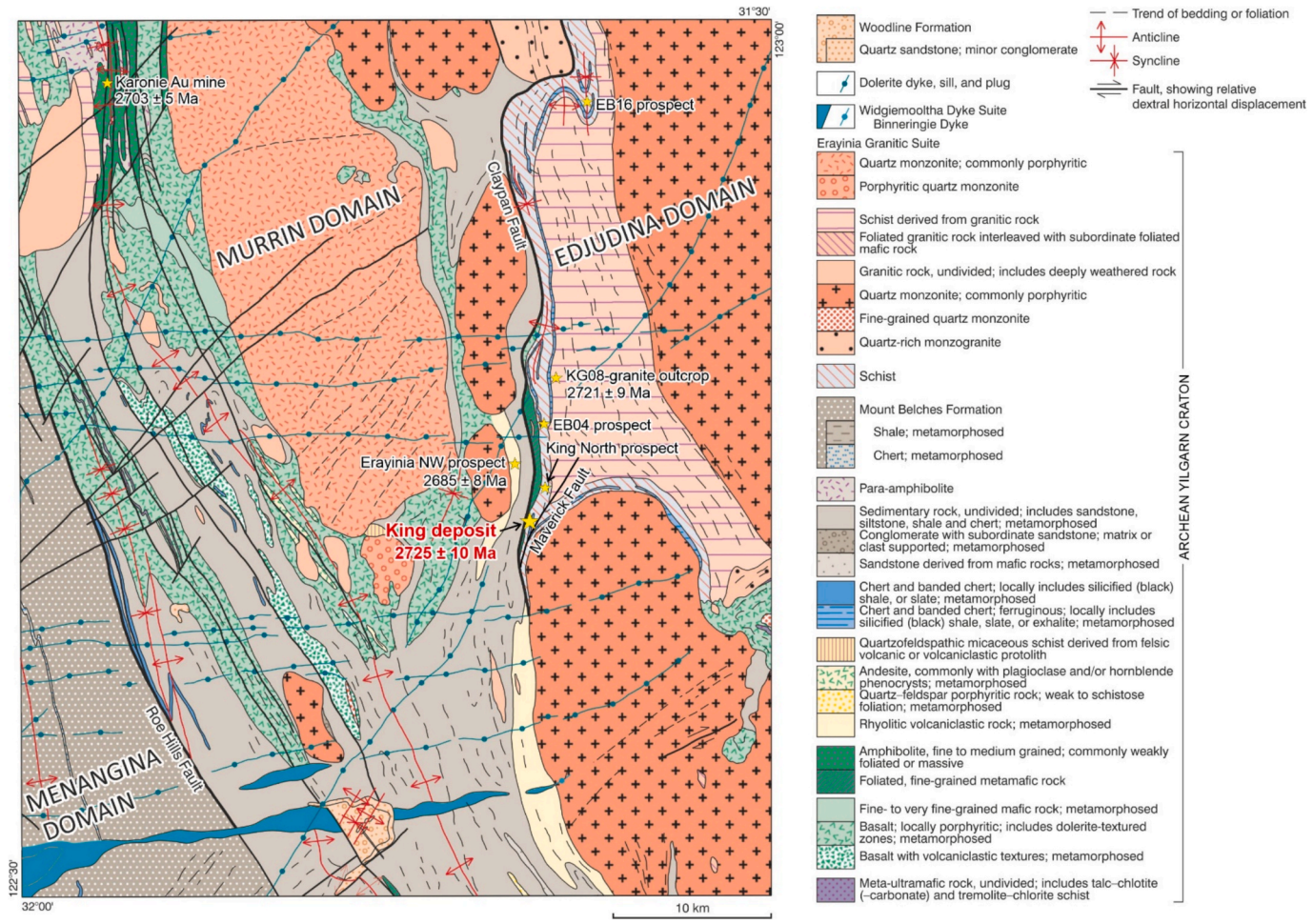

Fig. 3. Geological map of Erayinia region highlighting the location of the King deposit and nearby prospects (modified after Jones, 2007).

amphibole-quartz schist), calc-alkaline mafic metavolcanics (i.e., garnet amphibolite), and metasedimentary rocks (i.e., calcite-muscovite-quartz schist).

The stratiform massive sulfide orebody, is composed predominantly of pyrite and pyrrhotite with minor sphalerite, chalcopyrite and galena, is hosted within the upper felsic unit (Fig. 5a), directly beneath the metaexhalite horizon. However, it is unclear if the massive sulfide orebody formed through largely an exhalative or replacive processes just below the seafloor. Clasts of felsic host rocks in the massive sulfides might indicate subseafloor replacement processes (Hollis et al., 2019b), though this might also be due to the extensive recrystallization and/or milling of wall-rocks during latter deformation. Stringer sulfide mineralization hosted by felsic metavolcanic footwall is dominated by pyrite-sphalerite-pyrrhotite vein-veinlets and become more chalcopyrite rich with various tellurides towards the deep mafic metavolcanic footwall unit (i.e., garnet amphibolite; Hollis et al., 2019b; Dana et al., 2025). The entire stratigraphic sequence has been intruded by at least two generations of quartz-feldspar porphyry sills, several monzonite-granite intrusions (Fig. 5), and later-stage dolerite dikes. Further mineralogical and geochemical details are available in Kelly et al. (2024) and Dana et al. (2025).

3. Samples and analytical methods

3.1. Mineralogical characterization

Petrographic observations of thirty-three samples were performed using a Leica DMLP polarizing microscope equipped with a DFC 420C camera. Several representative samples were further characterized using a Carl Zeiss SIGMA HD VP Field Emission scanning electron microscope (SEM) at the University of Edinburgh, UK, equipped with an Oxford AZtec ED X-ray analysis. The analytical conditions were set as follows: accelerating voltage 15 kV, working distance 7 mm, beam current 20nA. A pure metallic cobalt standard was used for calibration.

3.2. U–Pb geochronology

Four samples of granitoid intrusions and one felsic metavolcanic footwall host rock (i.e., upper chlorite-muscovite-quartz schist) were sent to Geotrack Mineral Services, Australia, for zircon separation by heavy liquids and magnetic separation. The zircon separates were thermally annealed at 900 °C for 48 h, mounted in epoxy and then prepared for cathodoluminescence (CL) imaging. The CL imaging was performed using the same SEM instrument as those for mineralogical characterization, that is also equipped with a Centaurus CL detector. Additionally, one sample of granitoid intrusion and one sample from the mafic-derived metasedimentary footwall unit (i.e., biotite-muscovite schist) were prepared for titanite U–Pb dating.

The isotopic ratios and trace element concentrations of both zircon and titanite were analyzed by laser ablation-inductively coupled plasma-mass spectrometry (LA–ICP–MS) at the Institute of Geochemistry and Petrology, ETH Zurich, Switzerland, using a RESOlution S-155 (ASI/Applied Spectra) 193-nm ArF excimer laser ablation system attached to an Element XR (Thermo) sector-field ICP-mass spectrometer. The ablation spot diameters were set at 19 μm for zircon and 29 μm for titanite. The laser fluence and repetition rate for zircon were set at 2 J

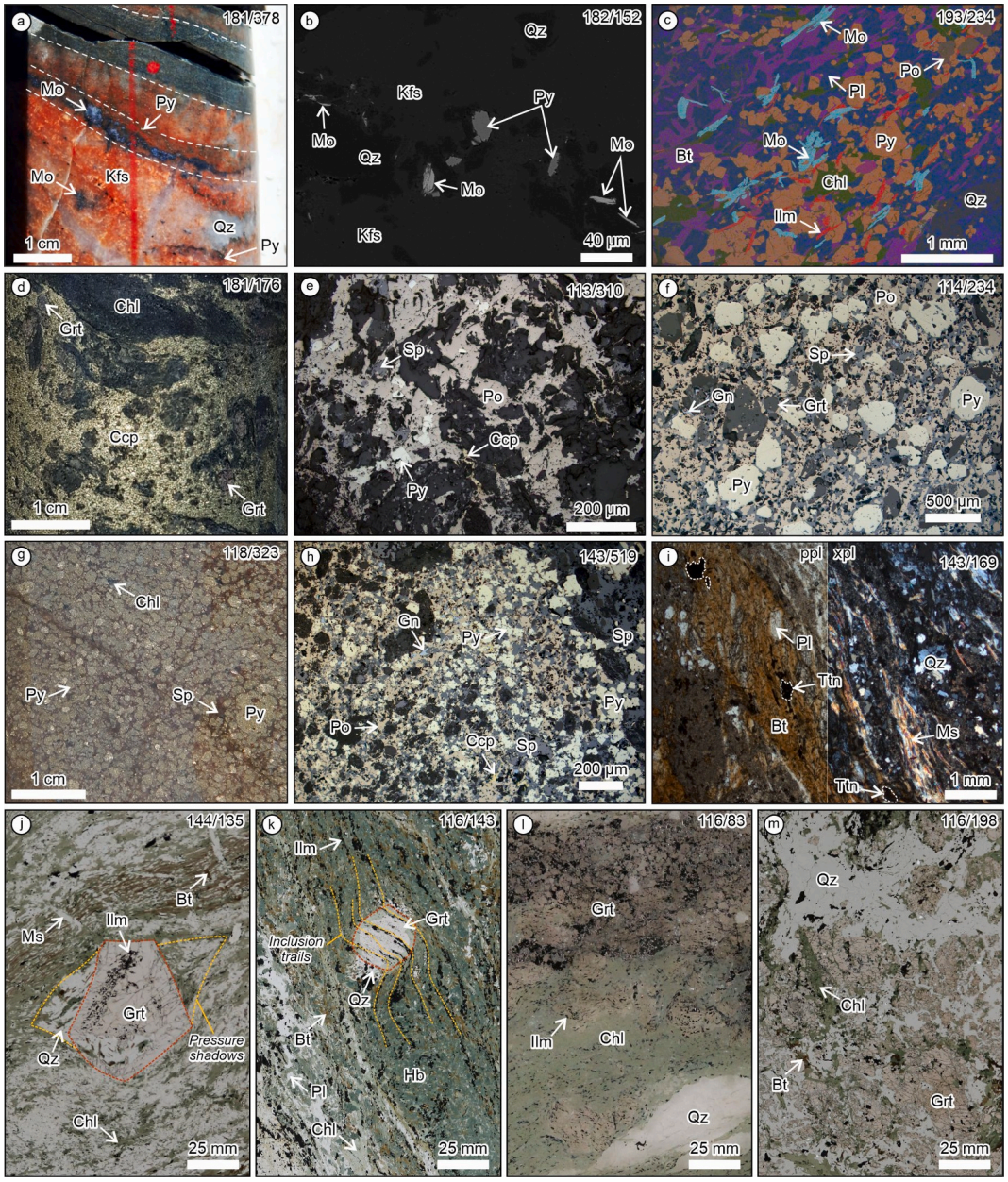

Fig. 4. Representative hand specimens and photomicrographs of samples used for geochronological analysis: (a–b) molybdenite in granitoid intrusions; (c) molybdenite along foliation within footwall lower felsic metavolcanic unit; (d) chalcopyrite mineralization hosted by footwall mafic metavolcanic unit; (e–h) mode of occurrences of pyrite and pyrrhotite within massive sulfide lens; (i) titanite grain hosted by footwall mafic-derived metasedimentary unit; (j–m) mode of occurrences of garnet within footwall mafic and felsic metavolcanic units.

cm^{-2} and 5 Hz, whereas for titanite they were set at 2 J cm^{-2} and 4 Hz. For zircon analyses, the GJ-1 zircon (Jackson et al., 2004) was used as primary reference material for U–Pb dating and validated using the Plešovice (337 Ma; Sláma et al., 2008), OG-1 (3467 Ma; Stern et al., 2009) and 91,500 (1065 Ma; Wiedenbeck et al., 1995) zircons as secondary reference materials. The MKED1 titanite (Spandler et al., 2016) was used as primary reference material for titanite U–Pb dating. The accuracy of titanite ages was assured by analyzing the following as unknowns: BLS (1050 Ma; Aleinikoff et al., 2007), 94–35 (52 Ma; Dana et al., 2023), Khan River (516 Ma; Mazoz et al., 2022), Bear Lake (1068 Ma; Mazoz et al., 2022), Otter West (148 Ma; Butler et al., 2002), Ectall West (92 Ma; Butler et al., 2002). All acquired data are available in Supplementary Table A1-A2, including metadata (Supplementary Table A3) with all relevant parameters after Horstwood et al. (2016).

For zircon analyses, data reduction was completed using Iolite 4 software with VizualAge (Paton et al., 2011; Petrus and Kamber, 2012). No common-Pb correction was applied but integration intervals were set to exclude inclusions, common Pb and discordant parts of the signal. After signal timing, only zircon spots with (nearly) concordant ages (<2% discordance) were used for the age calculation and the data were plotted on Wetherill concordia plots. The weighted mean $^{207}Pb/^{206}Pb$ age is reported to represent the crystallization age. All uncertainties on $^{207}Pb/^{206}Pb$ ages were reported as 2σ including σ_{sys} (i.e., long-term external uncertainty) which is in the range of 1.5 % for $^{207}Pb/^{206}U$ ages. This is composed of the uncertainty from the applied corrections, uncertainty of the decay constants, lacking common-Pb correction, the uncertainty on the true $^{207}Pb/^{206}U$ ratio of the primary standard GJ-1, and possible uncertainty from matrix effects. The Pb-loss age for the remaining discordant zircon spots were calculated using LeadLoss v.1.0 application (Mathieson et al., 2025) where the distribution was modeled

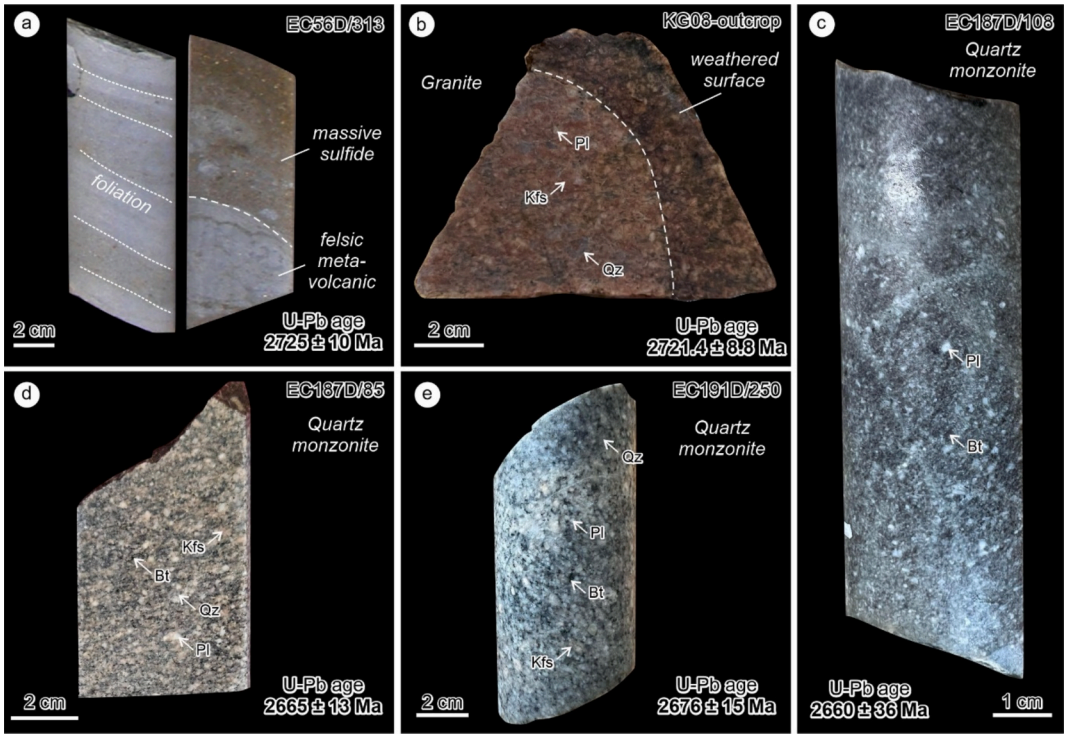

Fig. 5. Hand specimen of footwall felsic volcanic host-rock (a), *syn*-ore granite intrusion (b), and late quartz monzonite intrusions (c–e). A weighted mean $^{207}Pb/^{206}Pb$ zircon crystallization age is included for each sample.

over a range of 1–2600 Ma using a step size of 10 Myrs, 200 Monte Carlo simulations and penalization for invalid ages. The result is visualized in a Gaussian kernel density estimation (KDE) plot with smoothing bandwidth of 50.

For titanite analyses, isotopic ratios were quantified using the UcomPbine data reduction scheme available in Iolite 4 (Paton et al., 2010, 2011; Petrus and Kamber, 2012; Chew et al., 2014). Final titanite U–Pb ages were determined using IsoplotR v.6.5 (Vermeesch, 2018) via linear regressions on Tera-Wasserburg concordia plots with lower intercept inferred to represent the titanite crystallization age. Systematic uncertainties were propagated on final ages by quadratic addition of (i) the lower intercept age obtained using IsoplotR and (ii) the long-term excess variance (1.0 %) composed of the uncertainty from the applied corrections, uncertainty of the decay constants, uncertainty on the true $^{206}Pb/^{238}U$ ratio of the primary standard MKED1, and possible uncertainty from matrix effects.

3.3. Lu–Hf geochronology

A total of four representative samples (Fig. 5) consisting of three mafic footwall units (i.e., two garnet amphibolite and one biotite-muscovite schist) and one felsic footwall unit (i.e., lower chlorite-muscovite-quartz schist) were prepared as polished thin sections for *in situ* Lu–Hf analysis at Adelaide Microscopy, University of Adelaide. The analysis was carried out using an Agilent 8900x ICP–MS/MS, coupled to a RESOlution-LR ArF excimer (193 nm) laser ablation system. Details of the analytical conditions followed those described in Simpson et al. (2021) and Simpson et al. (2023). The ^{175}Lu isotope was measured as a proxy for ^{176}Lu, $^{176+82}Hf$ and $^{178+82}Hf$ were measured as mass-shifted reaction products for ^{176}Hf and ^{177}Hf, respectively. Isotopic ratios were calibrated to repeatedly measured NIST-610 glass in the LADR software (Norris and Danyushevsky; 2018). The Högsbo garnet was used to correct the Lu/Hf ratios for matrix-dependent fractionation and BP-1 (1745 ± 14 Ma; Lane 2011; Glorie et al., 2024) and Heftetjern (930.3 ± 1.0 Ma; Glorie et al., 2024) garnet secondary reference material were used to verify the accuracy of the calibration. Measured Lu–Hf dates are 1747 ± 18 Ma and 929.6 ± 6.5 Ma, respectively. All data and *meta*-data are available in Supplementary Tables A4-A5. For each sample and reference material, inverse isochron Lu–Hf dates were calculated in IsoplotR v.6.5 (Vermeesch, 2018), based on the matrix-corrected $^{176}Lu/^{176}Hf$ and $^{177}Hf/^{176}Hf$ isotopic ratios, their 2SE uncertainties (95 % confidence intervals), and the calculated uncertainty correlations. Inverse isochrons were chosen over normal isochrons as they provide a more rigorous means for inspecting datasets with strong uncertainty correlations (Li and Vermeesch, 2021). The uncertainties for the isochron dates are reported in the 95 % confidence interval including all sources of analytical uncertainty and decay constant (σ_{sys}).

3.4. Re–Os geochronology

3.4.1. Isotope dilution and negative thermal ionization mass spectrometry (ID–N–TIMS)

Three pure molybdenite mineral separates were prepared for Re–Os analysis utilizing a room temperature HF separation method (Lawley and Selby, 2012). The isotopic compositions were measured via ID-N-TIMS using Faraday collectors at the Durham Geochemistry Center of Durham University. The full details of the analytical protocol and data handling follow those described in Li et al. (2017). In brief, sample and tracer solution (^{185}Re + normal Os) were digested and equilibrated in a carius tube at 220°C for 24 h. The Re and Os fractions were isolated and purified using solvent extraction-anion chromatography, and solvent extraction-microdistillation protocols, respectively. Although negligible all Re–Os data were blank corrected, with the Re and Os blanks for the study being 2.3 and 0.5 pg (n = 1), respectively. The molybdenite Re–Os model age was calculated using the equation $t = \ln(^{187}Os/^{187}Re + 1)/\lambda$, in which λ is the decay constant (Smoliar et al., 1996). Quality of the measurements of the Re- and Os isotopic compositions was monitored by repeated analyses of in-house Re ($^{187}Re/^{185}Re = 0.5986 \pm 0.0014$, n = 855) and Os ($^{187}Os/^{188}Os = 0.16098 \pm 0.00013$, n = 147). Uncertainties are reported at the 2σ level and include all sources of analytical

uncertainty and that of the decay constant.

3.4.2. Multicollector inductively coupled plasma mass spectrometry (MC–ICP–MS)

A total of twenty samples were prepared for Re–Os analysis comprising bulk massive sulfide possessing an almost equal mix of pyrite and pyrrhotite (n = 9), pure mineral separates of pyrite (n = 6), pyrrhotite (n = 4), chalcopyrite (n = 1). Three whole-rock molybdenite-bearing granitoid rocks (n = 2) and felsic metavolcanic footwall (n = 1) were also prepared. Coarse-grained pyrite, pyrrhotite and chalcopyrite were separated by handpicking while massive sulfide and molybdenite-bearing granitoids were crushed in bulk. The analytical procedures follow those previously described by Ohta et al. (2022) and further detailed in Dana et al. (2023). For each sample, ~0.4 g powder, together with a tracer solution of ^{185}Re and ^{190}Os were digested in 4 mL of inverse aqua regia in a Carius tube in an oven at 220 °C for 24 h. After cooling, the Carius tube was opened, and the solution was transferred to a 30-mL Teflon vial. Rhenium in the sample solution was then purified by two-step chromatography using Muromac AG1-X8 anion exchange resin after the Os isotope measurement. For the molybdenite-bearing samples, the ^{187}Os was quantified by comparing its intensity with ^{192}Os intensity that was assumed to be derived completely from Os standard solution as the spike. The Re and Os isotopic ratios were measured using a Neptune Plus Thermo Fisher Scientific MC-ICP-MS at the Ocean Resources Research Center for Next Generation (ORCeNG) of Chiba Institute of Technology (CIT). Osmium and Re isotope ratios were measured using sparging sample introduction and solution introduction into the glass ICP torch through a self-aspirating PFA nebulizer and a glass spray chamber, respectively. The Re–Os data were blank corrected using 2.32 ± 0.17 pg for Re and 0.126 ± 0.017 pg for Os, with a ^{187}Os/^{188}Os of 0.907 ± 0.017 (average ± 1SD). The blank corrections range from 0.005 to 3.3 % for Re and 0.002 to 6.6 % for Os. The average ^{187}Re/^{185}Re value for standard solution was 1.67381 ± 0.00027 (n = 11; 2SD), whereas the average ^{187}Os/^{188}Os value for the JMC standard solution was 0.10709 ± 0.00069 (n = 5; 2SD) in which both are consistent with previously published data (^{187}Re/^{185}Re = 1.6738 ± 0.0005; Re–Ir mixed standard solution Ohta et al., 2022; ^{187}Os/^{188}Os = 0.10684 ± 0.00015; JMC Os standard solution; Nozaki et al., 2012).

The Re–Os data for pyrite, chalcopyrite and pyrrhotite were evaluated using the modeling approach of Davies et al. (2018) to independently confirm data clustering and determine which dates and initials (Os_i) are significant. We used the R script of Davies et al. (2018) to run a model with 100 points for each sulfide aliquot, to capture the analytical uncertainty in each measurement, but assume that all 100 points belong to a single aliquot and therefore the same isochron. The parameters set at, "iterate = 50" and "random.effects = TRUE" test for the possibility that the data can be explained by up to five possible isochrons, using the expectation–maximization (EM) algorithm. Allowing up to 1,000 possible iterations of the EM algorithm to allow it to converge ("n:iter = 1,000"). Any variability in the initiation of the EM algorithm is accounted for by repeated 100 times ("n:rep = 100"). The Re–Os isochron dates determined using both normal and inverse linear

Table 1
Summary of Re–Os concentrations and isotopic ratios in stringer and massive sulfides samples from the King deposit.

Sample code	Mineral	Sample weight (g)	Re (ppb)	2SE	Os (ppt)	2SE	^{187}Os (%)	^{187}Re/^{188}Os	2SE	^{187}Os/^{188}Os	2SE	Rho	Model ages
31/154-PY	Pyrite	0.40	0.332723	0.000062	97.0	2.4	98.03	8823	229	404	13	0.825	2686 ± 51
114/222-PY*		0.40	0.042857	0.000069	12.1	1.5	96.78	8745	1871	379	87	0.927	2546 ± 215
181/467-PY		0.40	0.48767	0.00031	373.57	0.26	39.84	102.10	0.10	4.9069	0.0049	0.541	2730 ± 42
114/236-PY		0.41	0.190336	0.000078	60.99	0.52	91.67	1800	16	84.16	0.98	0.769	2738 ± 26
86/380-PY*		0.40	0.169461	0.000066	58.76	0.77	94.80	2737	34	143.4	2.6	0.693	3062 ± 43
56/325-PY*		0.40	0.009061	0.000013	2.60	0.45	86.18	1923	552	78	24	0.944	2382 ± 238
181/176-CP*	Chalcopyrite	0.40	2.06030	0.00051	557	32	99.85	138,530	10,232	5955	518	0.849	2526 ± 115
113/310-PO	Pyrrhotite	0.40	0.59525	0.00018	173.7	1.6	97.50	6623	50	299.9	3.3	0.676	2652 ± 30
113/311-PO*		0.40	0.50395	0.00011	156	21	97.14	5714	676	287	45	0.746	2935 ± 301
173/293-PO		0.40	0.291787	0.000042	93.08	0.56	90.08	1501.3	7.5	68.50	0.62	0.553	2652 ± 74
116/175-PO*		0.41	0.057503	0.000017	17.5	3.7	98.51	28,583	15,650	1328	765	0.951	2725 ± 475
143/519-MS	Bulk massive sulfides	0.41	0.134747	0.000033	45.55	0.39	85.65	984.0	8.4	45.31	0.48	0.807	2682 ± 24
114/234-MS*		0.40	0.13715	0.00004	47.2	1.5	85.58	964	30	45.1	1.9	0.738	2724 ± 79
55/348-MS*		0.40	0.16258	0.00022	49.7	1.4	96.80	5915	239	280	14	0.825	2773 ± 79
189/148-MS		0.40	0.30266	0.00035	131.67	0.26	67.25	330.03	0.85	15.318	0.047	0.667	2663 ± 35
118/323-MS		0.40	0.13816	0.00016	42.19	0.82	93.89	2823	82	129.8	4.5	0.834	2691 ± 53
59/175-MS		0.40	0.27562	0.00031	81.71	0.68	95.30	3642	50	164.4	2.6	0.851	2645 ± 27
56/338-MS		0.39	0.183268	0.000059	54.92	0.63	93.67	2572	28	116	2.0	0.626	2640 ± 39
116/427-MS*		0.40	0.119958	0.000027	39.93	0.37	88.01	1203	11	56.30	0.68	0.753	2729 ± 28
190/164-MS*		0.40	0.40599	0.00046	19,361	731	68.44	3.11	0.12	16.06	0.86	0.707	108071 ± 2100

Note: *excluded in the isochron age calculation; model ages calculated using an initial Os derived from the isochron, uncertainty including all sources of analytical uncertainty plus decay constant.

regressions (model 1: maximum likelihood) constructed using IsoplotR v.6.5 (Vermeesch, 2018; Li and Vermeesch, 2021). The uncertainties for Re–Os analysis are reported to two standard errors, with uncertainties for the isochron are reported in the 95 % confidence interval including all sources of analytical uncertainty and decay constant. Note that samples with more than 90 % radiogenic ^{187}Os are considered as low-level highly radiogenic sulfides (LLHR; Stein et al., 2000). Model dates were also calculated using initial Os derived from the respective isochron (i.e., pyrite-chalcopyrite = 0.156 ± 0.035; pyrrhotite = 0.67 ± 0.98; bulk massive sulfide = 0.347 ± 0.098) and the results are provided in Table 1.

3.5. Lead (Pb) isotopes

A total of six samples were crushed and coarse-grained galena was handpicked. Lead isotopes were measured using a Neptune Plus Thermo Fisher Scientific MC-ICP-MS coupled to a Teledyne-Cetac Technologies Aridus II desolvating nebulizer and an ESI SC-microautosampler with PFA-50 nebulizer tip at the National Environmental Isotope Facility – Geochronology and Tracers Facility (NEIF-GTF) of British Geological Survey (BGS) Keyworth. Details of analytical conditions are provided in the Supplementary Table A6. The acquisition consisted of 50 ratios, collected at 8.6 s integrations, following a 60 s de-focused baseline measurement made at the beginning of each analytical session. The results were calibrated using NBS981 as primary reference material and are corrected (normalized) relative to the known values from Thirlwall (2002). The uncertainties were propagated relative to the reproducibility of the session NBS 981, to take into account the uncertainties associated with the normalization process. Lead isotopic calculations including model age, model source μ ($^{238}U/^{204}Pb$), time-integrated κ ($^{232}Th/^{238}U$), and initial Pb isotope ratios evolution models were performed using the PbIso web app (Armistead et al., 2023).

4. Results

4.1. Zircon U–Pb dates

4.1.1. Felsic metavolcanic host rock

Zircon grains (n = 19) from the footwall upper chlorite-muscovite-quartz schist (EC56D/313 m), are mostly euhedral-subhedral (vary in size between 50 and 100 μm) with microfractures, and display oscillatory or sector zoning in CL images (Supplementary Fig. A1). Only 13 out of 45 analytical spots were concordant and yielded a weighted mean $^{207}Pb/^{206}Pb$ age of 2725 ± 10 Ma (MSWD = 0.74; Fig. 6a). The Pb-loss date was also calculated using the remaining discordant analyses and yielded an optimum date of ca. 270 Ma (95 % lower bound = 1 Ma; 95 % upper bound = 444 Ma; Supplementary Fig. A2).

4.1.2. Granitoid intrusions

Zircons from the selected granitoid intrusions are characterized by a large variability in size (60–200 μm), with some of the grains displaying textural evidence for metamictization (Supplementary Fig. A1). Two different ages from three granitoid intrusions were identified. The younger zircons have brighter CL than those that are older. The older granitoid intrusion of granite (i.e., KG08-outcrop; Fig. 5b) yielded a weighted mean $^{207}Pb/^{206}Pb$ age of 2721.4 ± 8.8 Ma (MSWD = 1.2; n = 21; Fig. 6b). The other two samples (i.e., quartz monzonite; Fig. 5d,e) show overlapping younger ages and yielded weighted mean $^{207}Pb/^{206}Pb$ dates of 2676 ± 15 Ma (MSWD = 1.2; n = 7; Fig. 6c) and 2665 ± 13 Ma (MSWD = 2.1; n = 11; Fig. 6d). A fourth sample (EC187D/108 m; Fig. 5c) yielded only 1 out of 17 concordant analytical spots, with an individual $^{207}Pb/^{206}Pb$ date of 2660 ± 36 Ma. The ca. 2670 Ma granitoid intrusions also contain inherited zircon grains that yielded overlapping weighted mean $^{207}Pb/^{206}Pb$ dates of 2745 ± 19 Ma (MSWD = 0.15; n = 2; EC191D/250 m) and 2738 ± 22 Ma (MSWD = 1.5; n = 2; EC187D/85 m). The Pb-loss date was also calculated using the remaining discordant analyses and yielded an optimum age of 1 Ma, indicating recent lead loss event. A secondary peak Pb-loss date at ca. 1296 Ma was also identified from sample EC187D/108 m (Supplementary Fig. A2).

4.2. Titanite U–Pb dates

Magmatic titanite was analyzed in a late granitoid intrusion (EC191D/250 m) and yielded a lower intercept date of 2675 ± 42 Ma (MSWD = 2.6; n = 15; Fig. 6e), which is overlapping within uncertainty with the weighted mean zircon date from the same sample (2676 ± 15 Ma). In contrast, metamorphic titanite hosted by the footwall biotite-muscovite schist (EC143D/169 m; Fig. 4i) is significantly younger than the magmatic titanite and yielded a lower intercept dateof 1368 ± 87 Ma (MSWD = 1.9; n = 30; Fig. 6f).

4.3. In situ Lu–Hf garnet dates

Lu–Hf dates obtained for garnet porphyroblasts from footwall mafic units yield consistent dates, although precision is compromised for Lu-poor garnets. Garnet from the footwall biotite-muscovite schist (EC144D/135 m; Fig. 4j) has an average Lu concentration of 2.1 ppm and yielded an inverse isochron date of 2687 ± 54 Ma (MSWD = 1.4; n = 40; Fig. 7a). Average Lu concentrations of garnet from sample EC116/143 m (i.e., garnet amphibolite; Fig. 4k) is higher (11.9 ppm), and yielded an inverse isochron date of 2680 ± 28 Ma (MSWD = 1.3; n = 39; Fig. 7b). In contrast, garnet from sample EC166D/83 m, another garnet amphibolite with more garnet abundance than those in EC116D/143 m (Fig. 4l), has lower Lu concentration (ca. 1.60 ppm on average) and yielded a less precise (but within uncertainty) date of 2535 ± 133 Ma (MSWD = 1.3; n = 40; Fig. 7c). The lower chlorite-muscovite-quartz unit sample (EC116D/198 m; Fig. 4m) has a lower Lu concentration compared to the mafic units (ca., 0.69 ppm on average) and yielded an imprecise inverse isochron date of 2722 ± 219 Ma (MSWD = 0.92; n = 37; Fig. 7d).

4.4. Sulfides Re–Os dates

4.4.1. Stringer and massive sulfides

Rhenium-osmium analysis were carried out on sulfides from the stringer zone and massive sulfide ore lens of the King deposit (Table 1). Pyrite occurs as recrystallized euhedral grains and surrounded by interstitial chalcopyrite. Both minerals are overgrown by pyrrhotite, typically in equal abundance. The Re–Os abundance of pyrite ranges from ~ 0.009 to 0.3 ppb and ~ 2.6 to 374 ppt, respectively. The chalcopyrite sample from a stringer vein recrystallized into the regional foliation hosted by mafic metavolcanic footwall unit (i.e., garnet amphibolite; Fig. 4d) has the highest Re abundance (~2.1 ppb) with 99.9 % radiogenic Os and yielded a nominal Re–Os model date of 2526 ± 115 Ma using an initial Os derived either from pyrite or pyrrhotite isochrons (discussed below). All the Re–Os pyrite data yielded an isochron date of 2790 ± 25 Ma (MSWD = 63; n = 6). A similar date is determined including the co-genetic chalcopyrite (2784 ± 24 Ma; MSWD = 54). Yet, the date is older and outside of uncertainty with the date of the felsic volcanic footwall that hosts the massive sulfide orebody (U–Pb zircon age = 2725 ± 10 Ma).

Our single analysis of chalcopyrite, and some pyrite samples, show scatter about the linear regression, which is clearly shown on an inverse isochron plot (Supplementary Fig. A3a). The dataset was further evaluated using the cluster analysis of Davies et al. (2018). Four Re–Os data clusters were identified (Supplementary Fig. A3b). Amongst the four clusters, only “cluster 2” provides geologically realistic gross Re–Os date and initial $^{187}Os/^{188}Os$ (Os_i) estimates (ca. 2732 Ma; modelled Os_i = 0.14; 33 % of the data; samples 181/467-PY and 114/236-PY). The Re–Os isochron date then computed using three defining samples based on inverse isochron and cluster analysis (i.e., samples 181/467-PY; 114/236-PY; 31/154-PY) and excluding the chalcopyrite and two pyrite

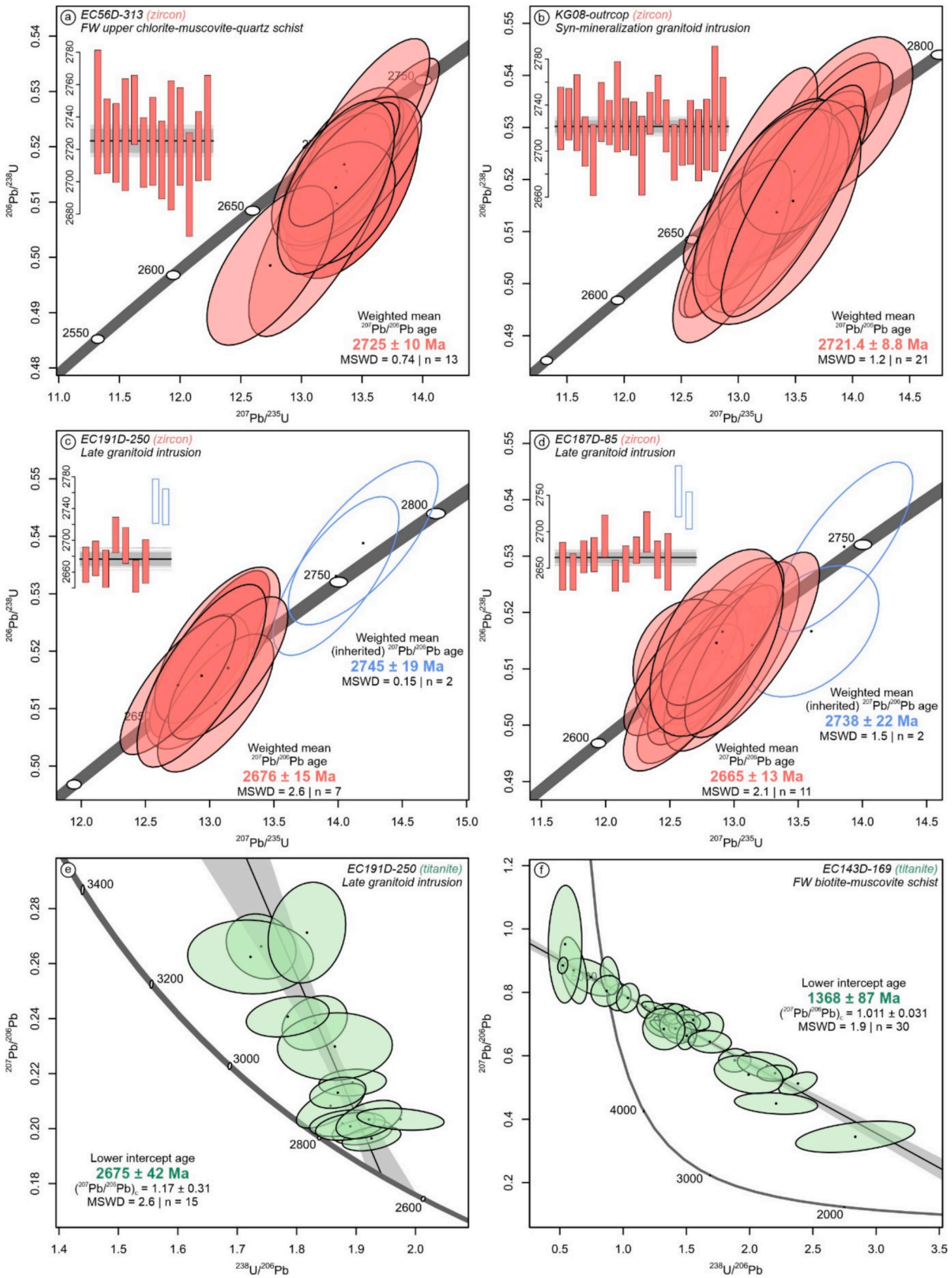

Fig. 6. Zircon Wetherill (a–d) and titanite Tera-Wasserburg (e–f) U–Pb concordia plots highlighting the age of felsic volcanic host-rock, syn- and post-ore intrusions as well as fault reactivation during Mesoproterozoic orogen. Note that the red label represents the crystallization ages whereas the blue label represents the xenocrystic zircon ages.

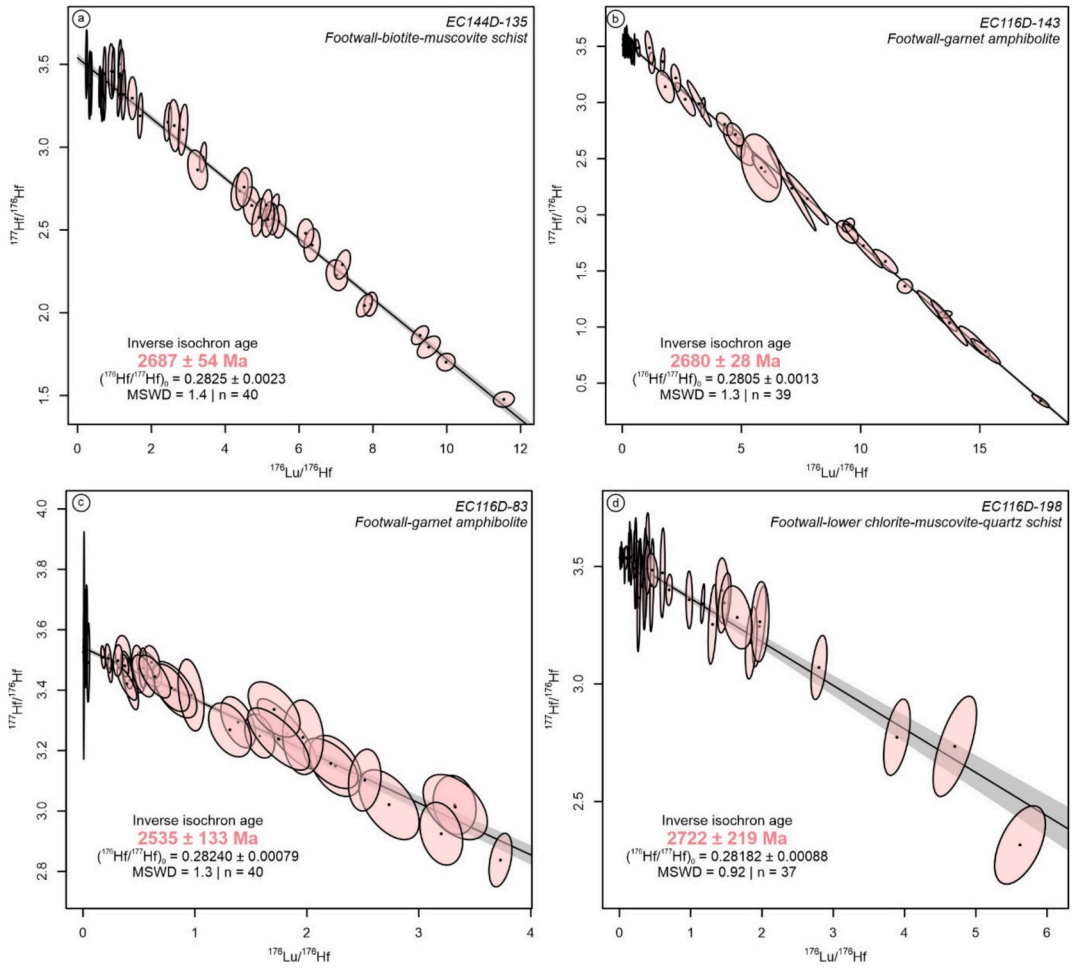

Fig. 7. Inverse isochron plots (Lu–Hf) of garnet from mafic (a–c) and felsic (d) volcanic footwall at King deposit.

samples (i.e., 86/380-PY and 56/325-PY). The Re–Os data for the four pyrite samples yielded an isochron date of 2730 ± 26 Ma (MSWD = 4; Os_i = 0.156 ± 0.035).

Paragenetically, pyrrhotite postdates euhedral pyrite and is intergrown with recrystallized chalcopyrite. It has Re abundances between ~ 0.06 to 0.60 ppb and Os abundances from ~ 18 to 174 ppt. The Re–Os data for the four pyrrhotite samples yielded an isochron date of 2654 ± 32 Ma (MSWD = 1.8) with an Os_i of 0.62 ± 0.97 (Fig. 8c). As performed for pyrite, cluster analysis of Davies et al. (2018) was also carried out for pyrrhotite dataset and three clusters were identified (Supplementary Fig. A3d). Of the three clusters, only "cluster 3" yields geologically plausible gross Re–Os dates and Os_i values (ca. 2645 Ma; modeled Os_i = 0.67; 49 % of the data; samples 113/310-PO and 173/293-PO). Additionally, two samples exhibit scatter from the isochron, especially 113/311-PO (Supplementary Fig. A3c). The isochron date then computed using the two defining samples suggested by the "cluster 3" yielded a similar isochron date (2652 ± 32 Ma; MSWD = 1; Os_i of 0.67 ± 0.98; Fig. 8c) which is consistent (within uncertainty) with "cluster 3" estimates, although a two-point isochron.

The Re–Os analysis was also carried out on bulk massive sulfides which are predominantly composed of pyrite and pyrrhotite in almost equal abundance with minor sphalerite, chalcopyrite and galena. The Re–Os abundances in the massive sulfides ranges from ~ 0.1 to 0.4 ppb and ~ 40 to 19,361 ppt, respectively. A total of nine massive sulfide samples yielded an isochron date of 2663 ± 21 Ma (MSWD = 200) with an Os_i of 0.39 ± 0.09 (Fig. 8d). However, four samples exhibit significantly scatter in the linear regression (Supplementary Fig. A3e). Excluding the Re–Os data from these samples, a similar isochron date of 2664 ± 23 Ma (MSWD = 3.7) and Os_i of 0.347 ± 0.098 is obtained (Fig. 8d). However, amongst four clusters obtained from the cluster analysis, none of the gross Re–Os date estimates match the isochron date (Supplementary Fig. A3f). The results from cluster analysis show either geologically meaningless gross Re–Os dates or unrealistic modelled Os_i estimates (cluster 1 = ca. 2610 Ma, modelled Os_i = 1.95; cluster 2 = 2749 Ma, modelled Os_i = -0.19; cluster 3 = ca. 2369 Ma, modelled Os_i = 15; cluster 4 = ca. 2819 Ma, modelled Os_i = -5.31).

4.4.2. *Molybdenite Re–Os chronology*

Molybdenite hosted by the footwall biotite-quartz schist (EC193D/324) occurs along the foliation associated with recrystallized magnetite, minor pyrite, pyrrhotite and rare chalcopyrite (Fig. 4c). Molybdenite in this sample was analyzed using both grain separates and bulk-rock digestion, and yielded model dates of 2655 ± 14 Ma and 2665 ± 19 Ma, respectively (Table 2).

Molybdenite in late granitoid intrusions, which crosscut the King stratigraphy, occur as either hosted by quartz veins (i.e., EC181D/378 m; Fig. 4a) or disseminated within the host-rock (i.e., EC182/152 m and EC85/51 m; Fig. 4b). In sample EC181D/378 m, molybdenite was also analyzed using both grain separates and bulk-rock digestion, yielding model dates of 2650 ± 15 Ma and 2663 ± 19 Ma, respectively (Table 2). Two additional molybdenite samples hosted by late granitoids yielded a model date of 2652 ± 14 Ma (EC182/152 m; mineral separate) and 2624 ± 19 Ma (EC85/51 m; bulk rock digestion).

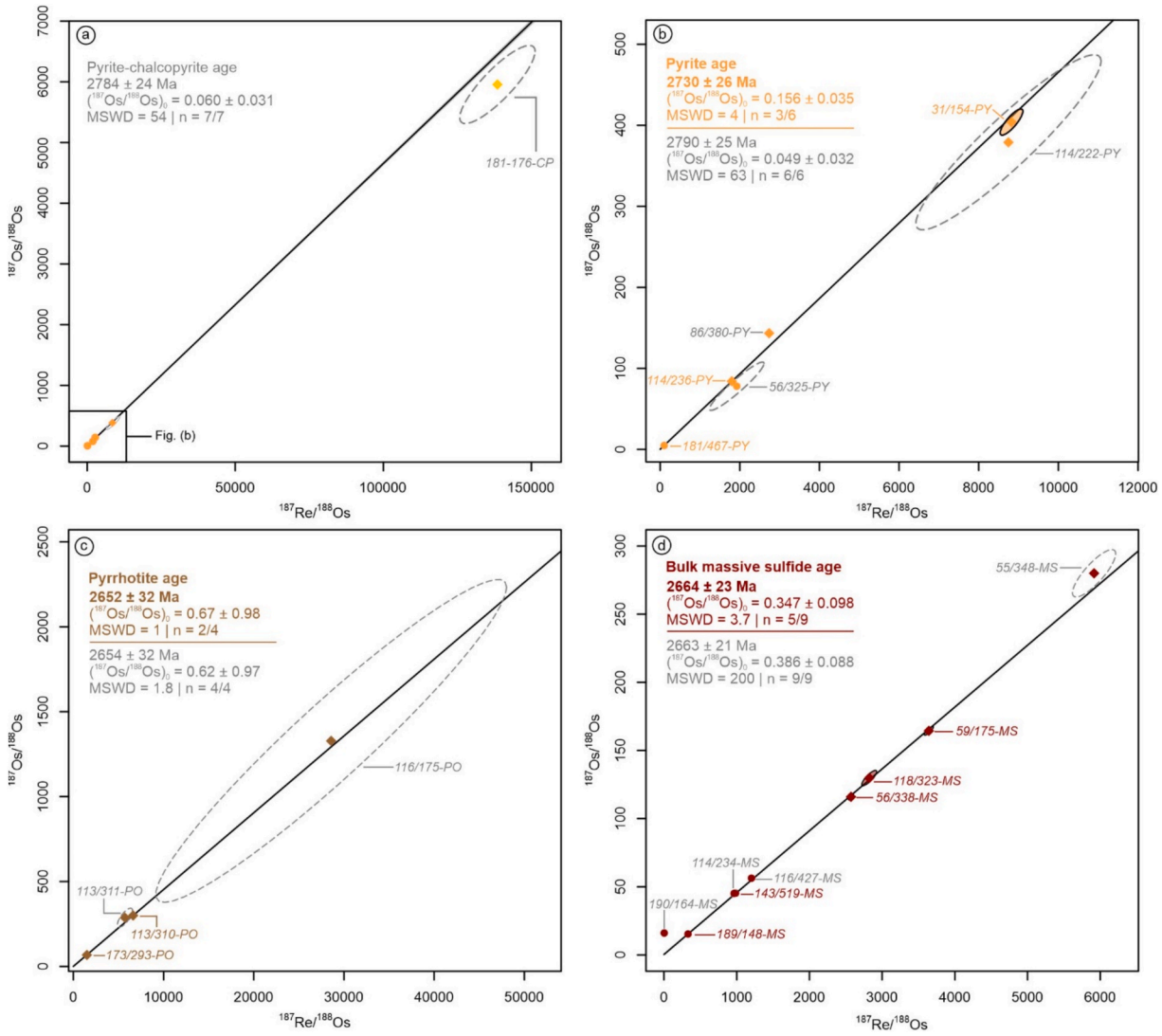

Fig. 8. Re–Os isochron diagrams of separated (a–b) pyrite-chalcopyrite, (c) pyrrhotite and (d) bulk massive sulfide samples.

Table 2
Summary of Re–Os concentrations and isotopic ratios in molybdenite samples from the King deposit.

Sample code	Host lithology	Method	Sample weight (g)	Re (ppm)	2σ	^{187}Re (ppm)	2σ	^{187}Os (ppb)	2σ	Model age (Ma)*
EC181D/378A	Late granitoid	N-TIMS-HF separation	0.021	220.25	0.82	138.43	0.52	6249	24	2650 ± 15
EC182/152	Late granitoid	N-TIMS-HF separation	0.021	15.27	0.06	9.60	0.04	433.60	1.36	2652 ± 14
EC193D/324A	Biotite-quartz schist	N-TIMS-HF separation	0.011	219.71	1.12	138.09	0.70	6246	28	2655 ± 14
EC181D/378B	Late granitoid	MC-ICP-MS-bulk digestion	0.22	0.002132	0.000015	0.0013402	0.0000098	0.060808	0.000085	2663 ± 19
EC85/51	Late granitoid	MC-ICP-MS-bulk digestion	0.049	0.04411	0.00032	0.02773	0.00026	1.239	0.0076	2624 ± 19
EC193D/324B	Biotite-quartz schist	MC-ICP-MS-bulk digestion	0.053	0.03219	0.00023	0.02023	0.00019	0.9183	0.0052	2665 ± 19

*Model age calculated from the simplified isotope equation [$t = \ln(^{187}Os/^{187}Re + 1)/\lambda$, where t = model age and $\lambda = ^{187}$Re decay constant], assuming no initial radiogenic Os; Uncertainty reported including all sources of analytical uncertainty plus decay constant.

4.5. Lead (Pb) isotopes of galena

The six analyzed galena samples have almost identical lead isotopic ratios ($^{206}Pb/^{204}Pb$ = 13.75–13.77; $^{207}Pb/^{204}Pb$ = 14.92–14.93; and $^{208}Pb/^{204}Pb$ = 14.97–14.98) (Table 3; Fig. 9). Using the Pb evolution model for the Yilgarn Craton (i.e., EGST) of Zametzer et al. (2022), which is a derivation from the Bulk Silicate Earth (BSE) Pb evolution model of Maltese and Mezger (2020), calculated model ages from the King deposit range from 2688 ± 23 to 2693 ± 16 Ma with μ ($^{238}U/^{204}Pb$) and κ ($^{232}Th/^{238}U$) values of 9.0 ± 0.1 and 4.1 ± 0.1,

Table 3
Lead (Pb) isotope composition of galena from the King deposit. Note that the uncertainty of model age (2σ) is calculated from analytical uncertainty only.

Sample code	$^{206}Pb/^{204}Pb$	2σ (%)	$^{207}Pb/^{204}Pb$	2σ (%)	$^{208}Pb/^{204}Pb$	2σ (%)	$^{207}Pb/^{206}Pb$	2σ (%)	$^{208}Pb/^{206}Pb$	2σ (%)	Model age (Ma) Model 1 *(Zametzer et al., 2022)*	Model 2 *(Thorpe, 1992)*	μ ($^{238}U/^{204}Pb$)	κ ($^{232}Th/^{238}U$)
187/286a	13.755	0.006	14.919	0.004	33.442	0.005	1.085	0.002	2.431	0.002	2692 ± 14	2718 ± 16	9.0	4.1
187/286b	13.754	0.005	14.918	0.004	33.438	0.004	1.085	0.001	2.431	0.002	2692 ± 14	2718 ± 15	9.0	4.1
25/181a	13.761	0.005	14.926	0.003	33.444	0.004	1.085	0.001	2.430	0.002	2692 ± 19	2718 ± 21	9.0	4.1
25/181b	13.760	0.005	14.925	0.003	33.441	0.004	1.085	0.001	2.430	0.002	2693 ± 16	2718 ± 17	9.0	4.1
27/96	13.767	0.005	14.927	0.003	33.445	0.004	1.084	0.001	2.429	0.002	2688 ± 21	2714 ± 23	9.0	4.1
56/338	13.752	0.006	14.915	0.004	33.438	0.005	1.085	0.001	2.432	0.002	2691 ± 13	2717 ± 16	9.0	4.1

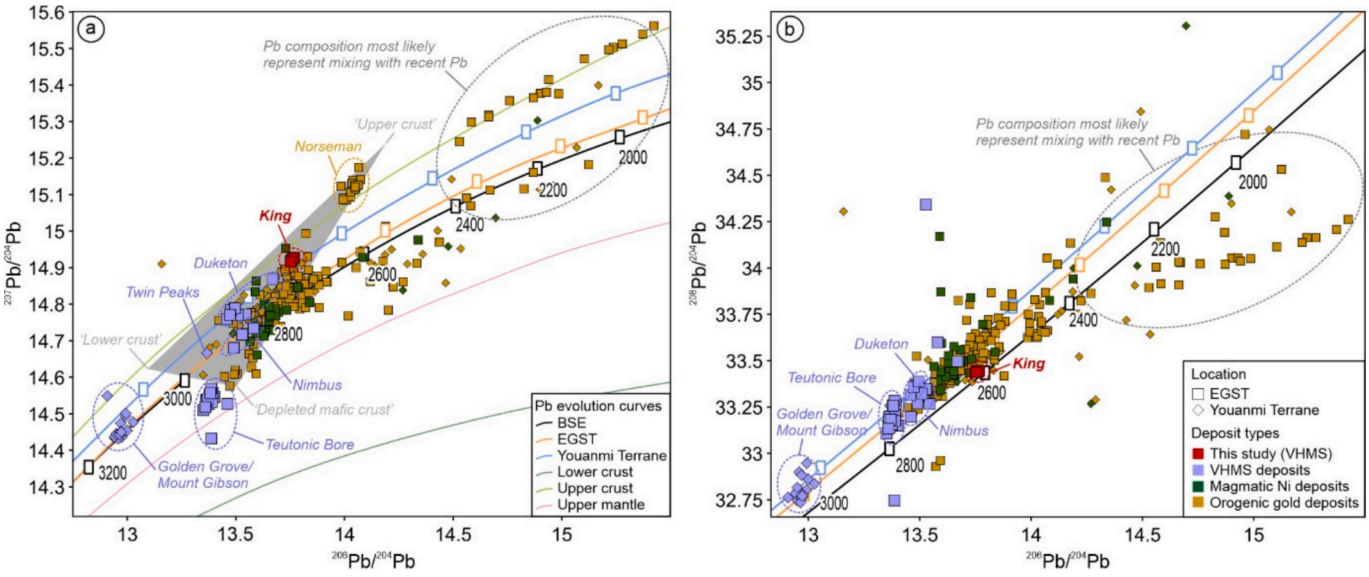

Fig. 9. Lead (Pb) isotope binary plots of (a) $^{206}Pb/^{204}Pb$ versus $^{207}Pb/^{204}Pb$ and (b) $^{206}Pb/^{204}Pb$ versus $^{208}Pb/^{204}Pb$. Pb growth curves: BSE (Maltese and Mezger, 2020); EGST and Youanmi Terrane (Zametzer et al., 2022); multi-stage for different crustal reservoirs after Kramers and Tolstikhin (1997). Note that grey triangle is the compositional Pb source model for the EGST after McNaughton and Groves (1996). Yilgarn regional Pb isotopes data from Zametzer et al. (2023) and references therein.

respectively (2σ from analytical uncertainty only). As a comparison, model ages were also calculated using the Archean sulfide model of Thorpe et al. (1992). The calculated Pb model ages using this model ranges from 2714 ± 23 to 2718 ± 21 Ma with μ and κ values of 9.3 ± 0.1 and 4.1 ± 0.1, respectively (2σ from analytical uncertainty only).

5. Discussion

5.1. Constraining the syn-genetic age of metamorphosed VHMS deposits

Although previous studies have suggested that Re–Os systematics in pyrite and molybdenite remain unaffected even by high-grade metamorphism (i.e., up to amphibolite facies) and intense deformation (e.g., Stein et al., 1999, 2001; Bingen et al., 2008; Nozaki et al., 2010; Wang et al., 2021), constraining the *syn*-genetic age of metamorphosed VHMS deposits remains challenging. Due to the large uncertainties involved, Re–Os ages can often overlap with later metamorphic events (e.g., Barrote et al., 2020b) or younger mineralization episodes that can overprint the original orebody (e.g., Lobanov et al., 2014; Tessalina et al., 2017). In this study, we have employed multiple geochronological approaches to constrain the age of the host stratigraphy, directly date VHMS mineralization at King, and younger magmatic and metamorphic events.

At King, the felsic volcanic footwall that hosts the massive sulfide orebody yielded a weighted mean U–Pb zircon age of 2725 ± 10 Ma, thus constraining the deposition age of the host stratigraphy. This age is consistent with our Re–Os isochron age of pyrite at 2730 ± 26 Ma, which was independently evaluated using the cluster analysis of Davies et al. (2018), and Pb model ages of galena (ca. 2714–2718 Ma) based on the Archean sulfide evolution model of Thorpe et al. (1992). Together these ages provide the best estimate for the timing of *syn*-genetic VHMS mineralization at King to ca. 2725 Ma (Fig. 10). This age is also in agreement with the timing of a granite intrusion emplacement (KG08; 2721 ± 9 Ma) ~ 10 km north of King, along strike of the footwall stratigraphy. In contrast, garnet Lu–Hf ages (most precise date: 2680 ± 28 Ma) suggest that Neoarchean prograde amphibolite-facies metamorphism is consistent with the M2 Yilgarn metamorphic event (i.e., low-P/moderate-T regional-contact type metamorphism; Goscombe et al., 2019), associated with widespread late high-Ca granite emplacement between ca. 2685–2665 Ma.

Numerous studies have shown that during prograde metamorphism, pyrite not only undergoes recrystallization but can also transform into pyrrhotite through desulfidation reactions (e.g., Toulmin and Barton, 1964; Craig and Vokes, 1993; Conn et al., 2019). This transformation is evident in the King deposit (Fig. 4e,f). Although the pyrite Re–Os system still preserves the *syn*-genetic VHMS age, the scatter observed in the Re–Os data for some of the samples suggests partial disturbance during metamorphism. Since pyrrhotite forms as a product of metamorphism, its formation age is expected to align with the timing of metamorphism. At King, pyrrhotite yields a Re–Os age of 2652 ± 32 Ma, which is

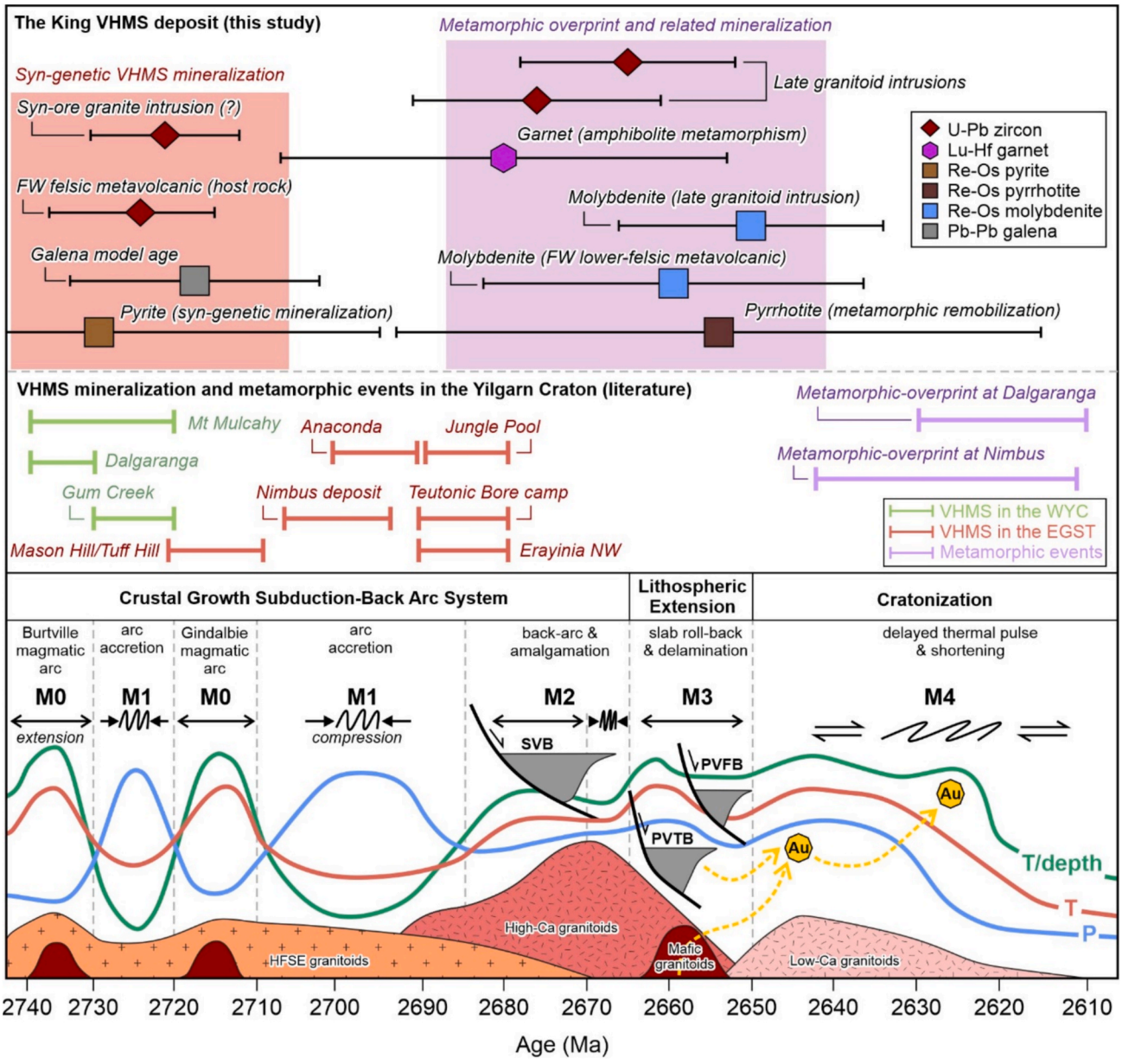

Fig. 10. Summary of geochronological data from the King deposit compared to regional tectono-magmatic and metamorphic events (modified from Goscombe et al., 2019) and timing of mineralization of other VHMS deposits. Note that the P, T, and T/depth curves are indicating relative values in which T/depth green curve is the apparent geothermal gradient. Abbreviations: SVB: *syn*-volcanic clastic basin; PVTB: post-volcanic turbiditic basin; PVFB: post-volcanic fluvial basin; WYC: Western Yilgarn Craton; EGST: Eastern Golfields Superterrane.

consistent with the age of prograde metamorphism (M2). As a result, the Re–Os age obtained from bulk massive sulfide ore, composed predominantly of pyrite and pyrrhotite, represents an average between the two minerals, yielding a geologically meaningless 'mixed' isochron age of 2664 ± 23 Ma. This is also evidenced by the cluster analysis in which none of the results match with the isochron age. This slightly younger age also implies that Re–Os budget in the bulk massive sulfide samples is controlled mostly by the pyrrhotite than pyrite. The mineral separates also demonstrate that in part the pyrrhotite is more Re–Os enriched than pyrite (Table 1). Whilst several studies have proposed that bulk massive sulfide ore Re–Os dating can provide reliable ages for mineralization in VHMS deposits (e.g., Mathur et al., 1999; McInnes et al., 2008; Nozaki et al., 2010), our findings demonstrate that this approach may not be applicable for deposits affected by high-grade metamorphism. Therefore, we recommend that in metamorphosed VHMS deposits, a separate pyrite fraction should be evaluated to obtain robust *syn*-genetic mineralization ages. Although the Re–Os systematics in pyrrhotite may be susceptible to disturbance during amphibolite-facies metamorphism due to its lower closure temperature (300–400 °C; e.g., Brenan et al., 2000; Nozaki et al., 2010; Rooney et al., 2024) compared to pyrite (>600 °C; e.g., Brenan et al., 2000), this does not render the pyrrhotite age meaningless. Our study demonstrates that the pyrrhotite age aligns with the garnet Lu–Hf age, suggesting it can be a valuable constraint on the timing of prograde metamorphism and perhaps related metal remobilization events (e.g., DeGrussa deposit; Hawke et al., 2015).

Additionally, we also analyzed one chalcopyrite sample from the King stockwork/feeder zone that shows characteristics of LLHR sulfide. This chalcopyrite gives a significantly younger model age 2526 ± 115 Ma compared to pyrite and pyrrhotite (Fig. 8c). Whilst several previous studies have suggested that the Re–Os systematics in chalcopyrite may remain unaffected by greenschist facies metamorphism (e.g., Selby et al., 2009; Lawley et al., 2013; Zhimin and Yali, 2013), other studies

have argued that chalcopyrite is more susceptible to Re–Os disturbance than pyrite (e.g., Barra et al., 2003; Lijuan et al., 2014; Saintilan et al., 2021) and can be reset by greenschist metamorphism (e.g., Morelli and Creaser, 2007) and/or at higher P-T conditions. Chalcopyrite at King is strongly recrystallized and often intergrown with pyrrhotite, sphalerite and galena. Although only based on one sample, the significantly younger model age and deviation from the linear regression suggests that the chalcopyrite Re–Os systematics are reset and geologically meaningless due to Re loss or Os gain during metamorphism. This is likely the result of prograde M2 metamorphic temperatures (ca. 500–700 °C; Goscombe et al., 2019) being higher than the closure temperature of chalcopyrite (~500 °C; Lawley et al., 2013; Zhimin and Yali, 2013).

5.2. Younger mineralization overprints

As suggested by our Lu–Hf garnet ages, prograde amphibolite grade metamorphism around the King deposit took place at ca. 2680 Ma, which correspond to the Yilgarn M2 metamorphic event (ca. 2665–2685 Ma) of Goscombe et al. (2019). Previous studies have suggested that the M2 metamorphic events are associated with the emplacement of high-Ca granitoid intrusions across the Yilgarn Craton (e.g., Mikucki and Roberts, 2003; Goscombe et al., 2019). At King, this is evident from many late granitoid intrusions that cross cut the metamorphosed footwall and hanging-wall stratigraphy. Regional geochemical work by Hollis et al. (2019b) has confirmed that these late granitoid intrusions are classified as belonging to the high-Ca granitoids suite of Czarnota et al. (2010). The late quartz monzonite intrusions at King yield overlapping weighted mean U–Pb ages ranging from 2676 ± 15 to 2665 ± 13 Ma. These quartz monzonites also contain an inherited zircon component that yielded weighted mean U–Pb ages from 2745 ± 19 Ma to 2738 ± 22 Ma and likely derived from the volcanic sequences within the footwall stratigraphy. This is consistent with previous dating of a quartz monzonite intrusion from 4 km NW of King (Fig. 3) at Erayinia NW, that yielded a U–Pb crystallization age of 2686 ± 11 Ma with an inherited zircon age component at 2720 ± 12 Ma (supplementary data of Hollis et al., 2019b).

These younger granitoid intrusions also host minor molybdenite mineralization, either as disseminated grains or within narrow quartz-carbonate veins (Fig. 4a,b). Regardless of the mode of occurrence, all granitoid-hosted molybdenite yielded near identical ages (2663 ± 19 –2624 ± 19 Ma). Rare molybdenite was also identified along the main foliation within the footwall lower felsic volcanic unit (EC193D/324; Fig. 4c). Interestingly, this sample occurs near a splay of the Maverick Fault which is associated with abundant intrusions of quartz monzonite (Dana et al., 2025; Black Raven Mining, *pers. comm.*). Petrographic observations also reveal that this molybdenite mineralization overprinted the pyrite-chalcopyrite-pyrrhotite mineralization (Fig. 4c). As this molybdenite yielded a similar age (2665 ± 19 to 2655 ± 14 Ma), this suggests that the rare molybdenite mineralization present in the King footwall is also associated with late granitoid intrusions in the wider context of the regional M2 metamorphic event.

To summarize, we demonstrate here that although molybdenite occurs within the footwall stratigraphy and provides robust ages despite high grade metamorphism (i.e., up to granulite facies; e.g., Stein et al., 1998, 2000; Bingen and Stein, 2003), these do not necessarily represent the *syn*-genetic age of VHMS mineralization. As molybdenite is uncommon in VHMS deposits (Leybourne et al., 2022), detailed petrographic observations are crucial to understand the paragenetic sequences and assign each ore phase to the correct mineralization event (e.g., Rooney et al., 2024).

5.3. Proterozoic and Paleozoic U–Pb disturbance

Following the above metamorphic events, it is likely that the King deposit was affected by a major orogenic event during the Mesoproterozoic. This is hinted by a robust U–Pb titanite age of 1368 ± 87 Ma (Fig. 6f) from the biotite muscovite schist unit (i.e., footwall mafic metasedimentary). The titanite in this sample formed during retrograde metamorphism, replacing prograde ilmenite, and is probably just slightly younger than the garnet age (ca. 2680 Ma). Therefore, we interpret the Mesoproterozoic age of titanite as its closure age after the U–Pb system reopening due to later thermal fluctuation, rather than its crystallization age. It is important to note that the King deposit is located in the southernmost of the Kurnalpi Terrane and near the contact with a major fault zone associated with the Albany-Fraser Orogen (ca. 1345–1140 Ma; Clark et al., 2000; Kirkland et al., 2011). This orogen would have caused the reactivation of structures along major regional shear zones (Goscombe et al., 2019) and localized deformation of the King deposit.

Interestingly, this titanite age overlaps within uncertainty of our zircon Pb-loss age (ca. 1296 Ma) from a late granitoid intrusion (sample EC187/108 m). A previous study had suggested that an ancient Pb-loss event in the EGST occurred at ca. 600 Ma which was speculated to be associated with the emplacement of the Cosmo Newbery Dikes (Kirkland et al., 2017). In contrast, our consistent zircon Pb-loss and metamorphic titanite ages reveal an older Pb-loss event associated with the Albany-Fraser Orogeny during Mesoproterozoic in the southern Kurnalpi Terrane. During the initial stage of this orogeny, granulite facies metamorphism at ca. 1300–1291 Ma (Clark et al., 2000) was followed by the emplacement of widespread dyke swarms at ca. 1238–1203 Ma across the southern margin of Yilgarn (e.g., E– W trending Gnowangerup swarm; NE– SW trending Fraser swarm; Wingate et al., 2005). This may also have caused radiogenic-Pb loss via thermally driven Pb diffusion (Kirkland et al., 2017).

Additionally, it should be noted a slightly younger Pb-loss event occurred at ca. 270 Ma which is likely associated with extensional faults during sedimentary basin formation and subsequent fluid-driven alteration (e.g., Veevers et al., 2005; Eyles et al., 2006). However, given the high degree of metamictization of the zircon grains, Pb-loss may occur without the need for a distinct younger geological event. In any case, U–Pb disturbance in the EGST is predominantly associated with recent Pb-loss (Kirkland et al., 2017), which is also the case at King.

5.4. Source(s) of metals for Archean VHMS deposits in the Yilgarn Craton

Multiple studies have used $^{187}Os/^{188}Os$ isotope ratios to fingerprint the metal sources in VHMS deposits. While several studies have suggested that the mantle is the primary source of Os in VHMS deposits (e.g., Gannoun et al., 2003; McInnes et al., 2008; Barrote et al., 2021), others have argued for crustal sources (e.g., Lehmann et al., 2013; Norman, 2023), or that $^{187}Os/^{188}Os$ variations indicate the mixing between hydrothermal fluids and seawater (e.g., Terakado, 2001; Nozaki et al., 2010, 2013).

Using the Re–Os pyrite data that yielded the timing of VHMS mineralization, we can use the Os_i ratios to fingerprint the source of osmium and by inference the source(s) of metals in the King deposit. Calculated Os_i values based on the pyrite isochron (0.158 ± 0.035) are slightly higher than the chondritic mantle value at ca. 2.7 Ga (0.108–0.112; Bennett et al., 2002; Walker and Nisbet., 2002), and significantly lower than the estimated crustal derived $^{187}Os/^{188}Os$ ratios of the 2.7 Ga and older crust (1.05 ± 0.23; Peucker-Ehrenbrink and Jahn, 2001). As has been argued by other studies, Archean 2.7 Ga ocean water was likely significantly influenced by submarine high-temperature hydrothermal fluids (Hannah and Stein, 2013; Viehmann et al., 2015). Previous studies have suggested that the $^{187}Os/^{188}Os$ signature of Archean oceans ranged from ~ 0.11 to ~ 0.20 between 2.7 – 2.0 Ga (Hannah and Stein, 2013; Stein and Hannah, 2015; Schulz et al., 2021). It is likely that the Os_i value at King thus reflects the mixing between ore-forming fluids, where the Os was mantle derived (or leached from mafic footwall rocks), and seawater. Such processes have

been documented in many ancient (e.g., Beshi-type, Nozaki et al., 2013; Iberian Pyrite Belt, Munhá et al., 2005; Southern Urals, Tessalina et al., 2008) and modern VHMS systems (e.g., Zeng et al., 2014). In the Yilgarn Craton, the Nimbus deposit has similar Os_i value of 0.119 ± 0.09, suggesting the predominance of mantle-derived Os in the hydrothermal system with a contribution from seawater (Barrote et al., 2021).

Whilst the Os_i isotope ratios are indicative of mantle-seawater derived Os, our Pb isotope data from galena suggest instead a mixed signature between crustal and mantle derived Pb (Fig. 9a). At King, the calculated μ shows identical values of 9.0 ± 0.1, which is slightly more radiogenic compared to other VHMS deposits at Yilgarn Craton (e.g., Nimbus = 8.6–8.7; Teutonic Bore camp = 7.9–8.6; Golden Grove camp = 8.2–8.8; Mt Gibson = 8.5–9.0; data compiled by Zametzer et al., 2023 and references therein). Although, it has not been directly dated, VHMS prospects at Duketon (e.g., Mason Hills/Tuff Hills at ca. 2.71–2.72 Ma) shows similar μ values (8.9–9.0, Browning et al., 1987; Dahl et al., 1987) with those from King. The Pb isotope signatures at King are generally consistent with previous studies that suggested a mixture of mantle- and crustal-derived Pb, which could be either from the melting of pre-existing continental crust or felsic volcanic host-rocks (e.g., Hollis et al., 2017a; Zametzer et al., 2023). Our study demonstrates that Pb isotopes are likely more effective for fingerprinting the source of metal, while Os isotopes not only help identify the metal source but are also more sensitive to seawater influence, thereby supporting the discrimination between *syn*-genetic VHMS and metamorphic-related signature. This further implies that the Pb and Os isotopic systems retain pre-metamorphic signatures despite significant recrystallization during amphibolite facies metamorphism, consistent with observations from previous studies (e.g., Barrote et al., 2021; Nozaki et al., 2010; Wang et al., 2021). However, it is important to note that only the Os_i isotopic composition in pyrite preserves the *syn*-genetic signature, whereas pyrrhotite exhibits a more radiogenic signature, indicating substantial modification during metamorphism.

5.5. Regional metallogenic implications

A comprehensive study by Hollis et al. (2015) suggested that there are at least four episodes of VHMS mineralization in the Youanmi Terrane at ca. > 2.95, 2.82, 2.75 and 2.72 Ga. Each pulse is typically associated with widespread continental rifting and bimodal volcanism following extensive plume magmatism, the emplacement of large mafic complexes in the upper crust (Ivanic et al., 2010; van Kranendonk et al., 2013), shallow crustal partial melting, and the generation of HFSE-enriched dacitic to rhyolitic magmas (Hollis et al. 2015). These silicic magmas are often emplaced as large coeval HFSE-enriched granites in close proximity to the VHMS deposits (Champion and Cassidy, 2001; Hollis et al., 2015; Hayman et al., 2015; Barrote et al., 2020a).

Two distinct episodes of VHMS mineralization have been previously defined in the EGST. The first at ca. 2705–2700 Ma is associated with plume magmatism in the Kalgoorlie and Kurnalpi terranes and is host to the Nimbus Ag-Zn-(Au) deposit (12 Mt at 0.9 % Zn, 52 g/t Ag, 0.2 g/t Au; Hollis et al., 2017a; Barrote et al., 2020b), and the historic Anaconda occurrences (i.e. Rio Tinto, Crayfish Creek, Nangaroo) previously mined for Cu. Whereas the Anaconda occurrences were deposited in the deeper rift basins of the Kurnalpi Sequence, the Nimbus deposit formed in significantly shallower waters near the margin of the Kalgoorlie Terrane (Hollis et al., 2017a). Komatiites, high-Mg- and low-Th-basalts (i.e., characteristic of mantle plumes) have been recognized from these host sequences (Hollis et al., 2017a).

The second major event at ca. 2695–2680 Ma formed the Teutonic Bore camp (6.5 Mt at 5.6 % Zn, 0.9 % Cu, 85 g/t Ag, 0.4 g/t Au; IGO Ltd., 2017) in the Gindalbie region, from which the Teutonic Bore, Jaguar and Bentley deposits have been mined (Barrote et al., 2020a). A previous study has also constrained the age of host rock (ca. 2685–2680 Ma; U–Pb SHRIMP zircon; Hollis et al., 2019a) of a pyrite-rich VHMS mineralization (e.g., 4 m at 0.2 % Zn, 15 m at 0.1 % Cu in drillhole EC157D; Hollis et al., 2019a) in the Erayinia region ~ 4 km NW of the King deposit. However, it is important to note that this stratigraphy is part of the Murrin domain, and is significantly younger than the King sequence of the Edjudina domain.

Our U–Pb zircon crystallization age from the King footwall stratigraphy and pyrite Re–Os isochron age suggest that the King deposit was formed at ca. 2725 Ma and represents the first phase of VHMS mineralization in the KKR, predating the Nimbus and Teutonic Bore deposits by ~ 20 to 30 Myr. This also suggests a potential for VHMS mineralization elsewhere within the ca. 2.72 Ga felsic volcanic sequences across the EGST, opening new opportunities for future exploration. The formation of the King deposit coincided with the emplacement of *syn*-ore granite intrusions (e.g., 2721 ± 9 Ma; sample KG08). This is consistent with previous studies that suggested that occurrences of VHMS mineralization in the Yilgarn craton are spatially and temporally associated with HFSE-enriched granites (e.g., Hollis et al., 2015; Barrote et al., 2020a). Interestingly, U-Pb zircon geochronology from an intrusive tonalite at Outcamp Bore (25 km NNW of the Porphyry Au mine) suggests that in this region the old Kurnapi Sequence greenstone belt stratigraphy extends back to at least 2719 ± 5 Ma in age (Nelson, 1996, 1997). This intrusion is also HFSE-enriched (Blewett and Czarnota, 2007), suggesting the local stratigraphy is likely to be VHMS prospective.

Whereas VHMS occurrences in the Youanmi Terrane are distributed along the Cue zone, all major VHMS deposits in the EGST are distributed along the KKR and its margins (Fig. 1). The timing of VHMS mineralization at King appears to coincide with the final phase of VHMS mineralization in the Youanmi Terrane, observed in the Gum Creek greenstone belt (ca. 2725–2720 Ma at Altair, Bevan, The Cup; Hollis et al., 2017b). It also coincides with the arrival of the ca. 2.72 Ga plume that formed the Kambalda Sequence of the EGST as plume magmatism was focused along the margin of the Youanmi Terrane (now reflected by the Ida Fault Zone) where the crust was considerably thinner (Mole et al., 2015). Whilst the tectonic setting and geological evolution of the EGST has been remained contentious, here we prefer a newly proposed model that combines both plume magmatism and subduction (e.g., Witt et al., 2020; Schreefel et al., 2024; Masurel and Thebaud, 2024; Fig. 11a).

We propose that the King deposit formed during the incipient stages of this continental rifting process at ca. 2.72 Ga associated with the formation of the KKR (e.g., Witt et al., 2020; Jones, 2024; Schreefel et al., 2024; Masurel and Thébaud, 2024; Fig. 11b). Crustal thinning and mantle upwelling resulted in the partial melting of the upper to middle crust, reflected by the presence of FI to FII affinity rhyolites (Hollis et al., 2019a; Kelly et al., 2024; Dana et al., 2025), and the emplacement of similar granitic magmas into the uppermost crust as large coeval granitoids (e.g., KG08; 2721 ± 9 Ma). Only minor amounts of FIII affinity rhyolites have been recognized in the King sequence (Kelly et al., 2024). This contrasts with the felsic volcanic host rocks from the Teutonic Bore camp, which predominantly exhibit FIII affinity signatures and are interpreted to have formed through melting of hydrated basaltic crust at much shallower crustal levels (e.g., Hart et al., 2004; Piercey, 2011; Hollis et al., 2015; 2017).

Lead (Pb) isotope signatures from the King deposit are indicative of extensive hydrothermal circulation through evolved 'Youanmi-like' older upper crust. Fragments of this older (>2.72 Ga) basement are exposed across the Kalgoorlie and Kurnalpi terranes (e.g., Norseman-Wiluna greenstone belt; Fig. 2). As rifting progressed, extreme crustal thinning led to the deepening of the KKR system, and an increased juvenile mantle component to the crust (e.g., Huston et al., 2010, 2014; Zametzer et al., 2023; Fig. 11c,d), as reflected in the Pb isotope signatures from the ca. 2703 Ma Nimbus and ca. 2695 Ma Teutonic Bore deposits (Fig. 9). In any case, the VHMS deposits of the EGST occurred in an intra-oceanic environment, where seawater acted as a critical ore-forming fluid for initiating sulfide precipitation (i.e., indicated by the Os_i isotope signatures).

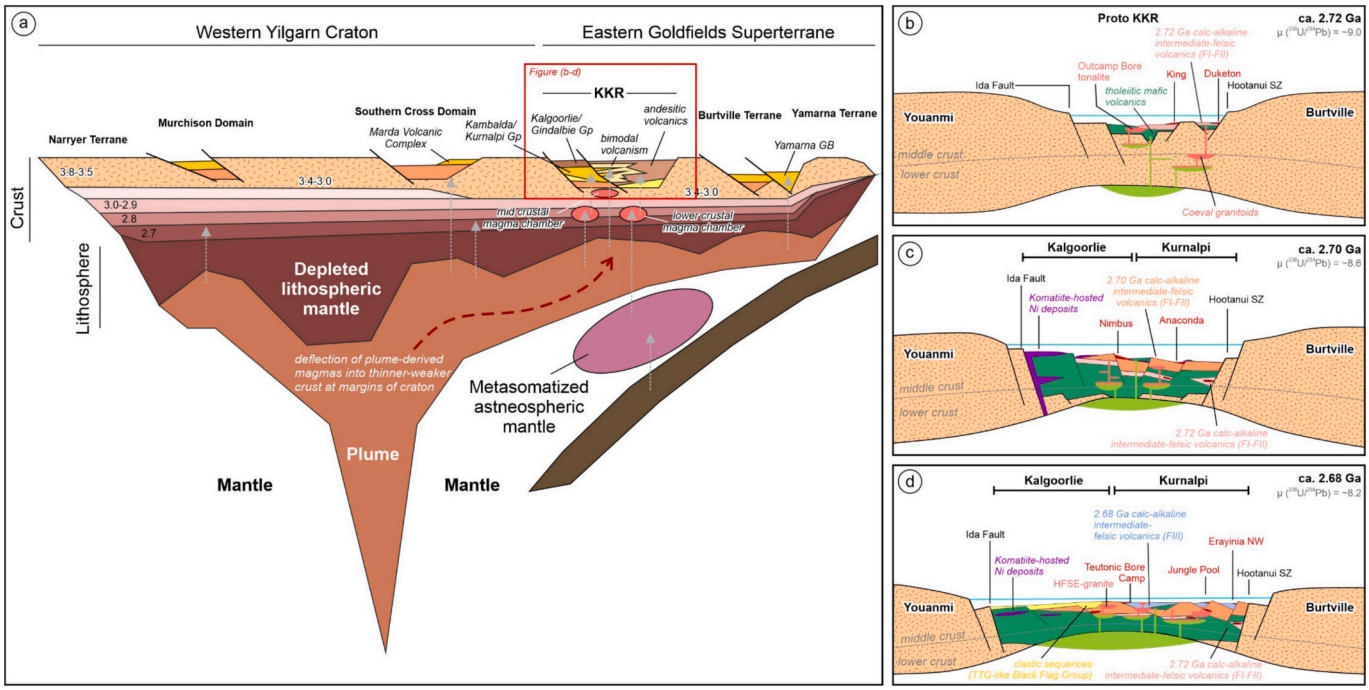

Fig. 11. (a) Tectonic setting of the Yilgarn Craton between 2.72 and 2.65 Ga (modified from Witt et al., 2020); (b–d) Schematic illustration of rifting phases in the KKR from ca. 2.72 to 2.68 Ga associated with the formation of VHMS deposits.

It is likely that the bimodal volcanism in the EGST was terminated shortly after the formation of the Gindalbie sequence (i.e., host to the Teutonic Bore VHMS camp) at ca. 2.67 Ga. Perhaps this also marked the switch from plume to subduction dominated tectonics associated with the onset of Kalgoorlie orogeny (e.g., Masurel and Thébaud, 2024). This period is also associated with the peak emplacement of high-Ca granitoids which also drove the M2 regional-contact metamorphism (e.g., Goscombe et al., 2019; Witt et al., 2020; Masurel and Thébaud, 2024). This metamorphism triggered local to regional metal remobilization and the formation of widespread orogenic gold mineralization (e.g., Goscombe et al., 2019). At King, prograde metamorphism is reflected by pyrrhotite formation, extensive sulfide recrystallization, and the presence of minor molybdenite mineralization associated with high-Ca granites.

6. Conclusions

The *syn*-genetic mineralization at the King deposit represents the oldest dated VHMS system in the Eastern Goldfields Superterrane of the Yilgarn Craton, formed around 2.73–2.72 Ga during the early stages of continental rifting linked to the development of the Kalgoorlie–Kurnalpi Rift. Subsequently, the deposit was overprinted by amphibolite facies metamorphism at approximately 2.68 Ga (constrained by *in situ* garnet Lu–Hf dating), coinciding with the emplacement of high-Ca granitoid intrusions (ca. 2.68–2.66 Ga), which also generated minor molybdenite mineralization (~2.65–2.66 Ga).

This study also demonstrates that the Re–Os isotopic signature of *syn*-genetic pyrite can be preserved through amphibolite facies metamorphism. This offers a new opportunity to directly date VHMS deposits affected by high-grade metamorphism in Archean cratons. In contrast, Re–Os dating of pyrrhotite reflects the timing of prograde metamorphism, offering a potential tool for constraining metal remobilization events. Therefore, in highly metamorphosed massive sulfide deposits where abundant pyrrhotite formed through pyrite desulfidation, bulk rock Re–Os dating is not reliable.

CRediT authorship contribution statement

Cendi D.P. Dana: . **Steven P. Hollis:** Writing – review & editing, Supervision, Methodology, Investigation, Funding acquisition, Conceptualization. **Lorenzo Tavazzani:** Writing – review & editing, Validation, Methodology, Investigation, Formal analysis. **Cyril Chelle-Michou:** Writing – review & editing, Validation, Methodology, Investigation. **Stijn Glorie:** Writing – review & editing, Validation, Methodology, Investigation. **Yusuke Kuwahara:** Writing – review & editing, Methodology, Investigation, Funding acquisition. **Kazuhide Mimura:** Writing – review & editing, Validation, Methodology, Investigation. **Moei Yano:** Writing – review & editing, Validation, Methodology, Investigation, Funding acquisition. **Junichiro Ohta:** Writing – review & editing, Validation, Methodology, Investigation. **David Selby:** Writing – review & editing, Methodology, Investigation, Formal analysis. **Yasuhiro Kato:** Writing – review & editing, Validation, Supervision, Funding acquisition. **Vanessa Pashley:** Writing – review & editing, Validation, Methodology, Investigation. **Megan James:** Writing – review & editing, Supervision, Resources, Funding acquisition. **Darryl Podmore:** Writing – review & editing, Supervision, Resources, Funding acquisition.

Declaration of competing interest

The authors declare that they have no known competing financial interests or personal relationships that could have appeared to influence the work reported in this paper.

Acknowledgements

This study is funded by a National Environment Research Council (NERC) Doctoral Training Partnership grant (NE/S007407/1) with additional funding and support provided by Black Raven Mining. Zircon-titanite U–Pb and molybdenite Re–Os dating were funded by the Hugh McKinstry Fund Student Research Grants (SRG 23-03) of the Society of Economic Geologists (SEG). Travel expenses during U–Pb analyses was supported by the Society for Geology Applied to Mineral Deposits (SGA) Mobility Grant and the European Association of Geochemistry (EAG)

Student Sponsorship awarded to CD. Sulfide Re–Os dating at CIT was funded by the Japan Society for the Promotion of Science (JSPS) KAKENHI grants 20H05658 to YK and 22K14637 to MY, with travel support from an E4 DTP ORVCF grant to the lead author. We thank Kana Ashida of CIT and Nicola Cayzer of University of Edinburgh for their assistance during Re–Os and SEM-EDS analyses, respectively. DS acknowledges the support of Geoff Nowell and Chris Ottley at Durham University. We thank Riquan Azri and Danny Johnson (*in memoriam*) of Black Raven Mining for their assistance during the fieldwork campaign. SG is supported by an Australian Research Council Future Fellowship (FT210100906). The authors thank Patrick Hayman and an anonymous reviewer for their valuable comments, and Tony Kemp for editorial handling.

Appendix A. Supplementary data

Supplementary data to this article can be found online at https://doi.org/10.1016/j.precamres.2025.107968.

Data availability

New data generated during this research are contained within the article and supplementary materials. Restrictions apply to the availability of the company drilling database.

References

Aleinikoff, R.P., Wintsch, R.P., Tollo, R.P., Unruh, D.M., Fanning, C.M., Schmitz, M.D., 2007. Ages and origins of rocks of the Killingworth dome, south-central Connecticut: Implications for the tectonic evolution of southern New England. Am. J. Sci. 307, 63–118. https://doi.org/10.2475/01.2007.04.

Araujo, S.M., Scott, S.D., Longstaffe, F.J., 1996. Oxygen isotope composition of alteration zones of highly metamorphosed volcanogenic massive sulfide deposits; Geco, Canada, and Palmeiropolis. Brazil. Economic Geology 91 (4), 697–712. https://doi.org/10.2113/gsecongeo.91.4.697.

Armistead, S.E., Eglington, B.M., Pehrsson, S.J., 2023. PbIso: an R package and web app for calculating and plotting Pb isotope data. Can. J. Earth Sci. 61 (1), 1–15. https://doi.org/10.1139/cjes-2023-0029.

Austin, J.M., Hayman, P.C., Murphy, D.T., Wingate, M.T.D., Lu, Y., Lowrey, J., Rose, K., 2022. The voluminous 2.81–2.71 Ga Goldfields Tholeiitic Super Event: Implications for basin architecture in the Yilgarn Craton and global correlations. Precambr. Res. 369, 106528. https://doi.org/10.1016/j.precamres.2021.106528.

Barley, M.E., Blewett, R.S., Cassidy, K.F., Champion, D.C., Czarnota, K., Doyle, M.G., Krapež, B., Kositcin, N., Pickard, A.L., Weinberg, F., 2006, Tectonostratigraphic and structural architecture of the eastern Yilgarn Craton. Australian Minerals Industry Association Report, P763/pmd*CRC Project Y1.

Barrote, V.R., McNaughton, N.J., Tessalina, S.G., Evans, N.J., Talavera, C., Zi, J.-W., McDonald, B.J., 2020a. The 4D evolution of the Teutonic Bore Camp VHMS deposits, Yilgarn Craton. Western Australia. Ore Geology Reviews 120, 103448. https://doi.org/10.1016/j.oregeorev.2020.103448.

Barrote, V.R., Tessalina, S.G., McNaughton, N.J., Jourdan, F., Hollis, S.P., Ware, B., Zi, J.-W., 2020b. 4D history of the Nimbus VHMS ore deposit in the Yilgarn Craton. Western Australia. Precambrian Research 337, 105536. https://doi.org/10.1016/j.precamres.2019.105536.

Barrote, V.R., Tessalina, S.G., McNaughton, N.J., Evans, N.J., Hollis, S.P., McDonald, B. J., 2021. Surge of ore metals in seawater and increased bio-activity: a tracer of VHMS mineralization in Archaean successions, Yilgarn Craton, Western Australia. Miner. Deposita 56, 643–664. https://doi.org/10.1007/s00126-020-00986-6.

Belford, S., 2010. Genetic and chemical characterisation of the host succession to the Archaean Jaguar VHMS Deposit. University of Tasmania, Hobart, Tasmania, p. 392p. PhD thesis (unpublished.

Bennett, V.C., Nutman, A.P., Esat, T.M., 2002. Constraints on mantle evolution from 187Os/188Os isotopic compositions of Archean ultramafic rocks from southern West Greenland (3.8 Ga) and Western Australia (3.46 Ga). Geochim. Cosmochim. Acta 66 (14), 2615–2630. https://doi.org/10.1016/S0016-7037(02)00862-1.

Beresford, S., Stone, W.E., Cas, R., Lahaye, Y., Jane, M., 2005. Volcanological controls on the localization of the komatiite-hosted N–Cu–(PGE) Coronet Deposit, Kambalda, Western Australia. Econ. Geol. 100, 1457–1467. https://doi.org/10.2113/gsecongeo.100.7.1457.

Bingen, B., Davis, W.J., Hamilton, M.A., Engvik, A.K., Stein, H.J., Skar, O., Nordgulen, O., 2008. Geochronology of high-grade metamorphism in the Sveconorwegian belt, S. Norway: U–Pb, Th-Pb and Re–Os data. Nor. J. Geol. 88, 13–42.

Bingen, B., Stein, H.J., 2003. Molybdenite Re–Os dating of biotite dehydration melting in the Rogaland high-temperature granulites, S Norway. Earth Planet. Sci. Lett. 208 (3–4), 181–195. https://doi.org/10.1016/S0012-821X(03)00036-0.

Blewett, R.S., Czarnota, K., 2007, Tectonostratigraphic architecture and uplift history of the Eastern Yilgarn Craton, Module 3: Terrane Structure, Project Y1-P763. Geoscience Australia Record 2007/15.

Bodorkos, S., Love, G.J., Nelson, D.R., Wingate, M.T.D., 2006, 179239: porphyritic metadacite, Montague Well; Geochronology Record 647. Geological Survey of Western Australia, 4p.

Brenan, J.M., Cherniak, D.J., Rose, L.A., 2000. Diffusion of osmium in pyrrhotite and pyrite: implications for closure of the Re–Os isotopic system. Earth Planet. Sci. Lett. 180 (3–4), 399–413. https://doi.org/10.1016/S0012-821X(00)00165-5.

Browning, P., Groves, D.I., Blockley, J.G., Rosman, K.J.R., 1987. Lead isotope constraints on the age and source of gold mineralization in the Archean Yilgarn Block. Western Australia. Economic Geology 82 (4), 971–986. https://doi.org/10.2113/gsecongeo.82.4.971.

Burton, K.W., Capmas, F., Birck, J.-L., Allègre, C.J., Cohen, A.S., 2000. Resolving crystallisation ages of Archean mafic–ultramafic rocks using the Re–Os isotope system. Earth Planet. Sci. Lett. 179 (3–4), 453–467. https://doi.org/10.1016/S0012-821X(00)00134-5.

Butler, R.F., Gehrels, G.E., Baldwin, S.L., Davidson, C., 2002. Paleomagnetism and geochronology of the Ecstall pluton in the Coast Mountains of British Columbia: evidence for local deformation rather than large-scale transport. J. Geophys. Res. 107 (B1). https://doi.org/10.1029/2001JB000270.

Cassidy, K.F., Champion, D.C., Krapez, B., Barley, M.E., Brown, S.J.A., Blewett, R.S., Groenewald, P.B., Tyler, I.M., 2006. A revised Geological Framework for the Yilgarn Craton, Western Australia. Western Australia Geological Survey, Record 2006 (8), 8p.

Cassidy, K.F., Champion, D.C., 2004, Crustal evolution of the Yilgarn Craton from Nd isotopes and granite geochronology: implications for metallogeny. In: SEG 2004, Predictive Mineral Discovery Under Cover, Muhling J. (Ed.), Centre for Global Metallogeny, The University of Western Australia 33, 317-320.

Champion, D.C., Cassidy, K.F., Budd, A., 2001, Overview of the Yilgarn magmatism: implications for crustal development. In: Cassidy et al. (Eds.) Characterization and metallogenic significance of Archaean granitoids of the Yilgarn Craton, Western Australia. MERIWA Report 222.

Champion, D.C., Cassidy, K.F., 2010, Granitic magmatism in the Yilgarn Craton: implications for crustal growth and Metallogeny. In: Yilgarn-Superior Workshop — Abstracts, Fifth International Archaean Symposium, 10 September 2010. Geological Survey of Western Australia, Record 2010/20, 12–18.

Champion, D.C., Cassidy, K.F., 2007, An overview of the Yilgarn Craton and its crustal evolution. In: Bierlein F.P., Knox-Robinson C.M. (Eds.), Proceedings of Geoconferences (WA) Inc. Kalgoorlie '07 Conference. Geoscience Australia Record 2007/14, 13-35.

Champion, D.C., Sheraton, J.W., 1997. Geochemistry and Nd isotope systematics of Archaean granites of the Eastern Goldfields, Yilgarn Craton, Australia: implications for crustal growth processes. Precambr. Res. 83, 109–132. https://doi.org/10.1016/S0301-9268(97)00007-7.

Chen, G., Chen, M., Ke, C., Tang, Y., 2023. Paleozoic VMS-type stratiform mineralization overprinted by Mesozoic vein-type mineralization in the Yushui copper deposit, eastern Guangdong, South China. Ore Geology Reviews 158, 105498. https://doi.org/10.1016/j.oregeorev.2023.105498.

Chen, S.F., Riganti, A., Wyche, S., Greenfield, J.E., Nelson, D.R., 2003. Lithostratigraphy and tectonic evolution of contrasting greenstone successions in the central Yilgarn Craton, Western Australia. Precambr. Res. 127, 249–266. https://doi.org/10.1016/S0301-9268(03)00190-6.

Chew, D.M., Petrus, J.A., Kamber, B.S., 2014. U–Pb LA-ICPMS dating using accessory mineral standards with variable common Pb. Chem. Geol. 363, 185–199. https://doi.org/10.1016/j.chemgeo.2013.11.006.

Chiaradia, M., 2023. Radiometric dating applied to ore deposits: theory and methods. In: Huston, D., Gutzmer, J. (Eds.), Isotopes in Economic Geology, Metallogenesis and Exploration, Mineral Resource Reviews. Springer, Cham, pp. 15–35. https://doi.org/10.1007/978-3-031-27897-6_2.

Clark, D.J., Hensen, B.J., Kinny, P.D., 2000. Geochronological constraints for a two-stage history of the Albany–Fraser Orogen. Western Australia. Precambrian Research 102 (3–4), 155–183. https://doi.org/10.1016/S0301-9268(00)00063-2.

Conn, C.D., Spry, P.G., Layton-Matthews, D., Voinot, A., Koenig, A., 2019. The effects of amphibolite facies metamorphism on the trace element composition of pyrite and pyrrhotite in the Cambrian Nairne Pyrite Member, Kanmantoo Group. South Australia. Ore Geology Reviews 114, 103128. https://doi.org/10.1016/j.oregeorev.2019.103128.

Craig, J.R., Vokes, F.M., 1993. The metamorphism of pyrite and pyritic ores: an overview. Mineral. Mag. 57, 3–18. https://doi.org/10.1180/minmag.1993.057.386.02.

Czarnota, K., Champion, D.C., Goscombe, B., Blewett, R.S., Cassidy, K.F., Henson, P.A., Groenewald, P.B., 2010. Geodynamics of the eastern Yilgarn Craton. Precambr. Res. 183, 175–202. https://doi.org/10.1016/j.precamres.2010.08.004.

Dahl, N., McNaughton, N.J., Groves, D.I., 1987, A lead-isotope study of sulphide associated with gold mineralization in selected gold deposits from the Eastern Goldfields of Western Australia. In: Ho, S.E., Groves, D.I. (Eds.), Recent Advances in Understanding Precambrian Gold Deposits. Geol. Dep. & Univ. Extens., Univ. W. Aust. Publ., 11, 189-201.

Dana, C.D.P., Hollis, S.P., Podmore, D., James, M., Azri, R., 2025. Using coupled bulk-rock geochemistry and short-wave infrared (SWIR) spectral reflectance data as rapid exploration tools in metamorphosed VHMS deposits: insights from the King Zn deposit, Yilgarn Craton. Western Australia. Mineralium Deposita 60 (6), 1117–1140. https://doi.org/10.1007/s00126-024-01342-8.

Dana, C.D.P., Agangi, A., Idrus, A., Chelle-Michou, C., Lai, C.-K., Ishida, M., Guillong, M., Gonzalez-Alvarez, I., Takahashi, R., Yano, M., Mimura, K., Ohta, J., Kato, Y.,

Simbolon, D.R., Xia, X.-P., 2023. The age and origin of the Ruwai polymetallic skarn deposit, Indonesia: evidence of cretaceous Mineralization in the Central Borneo Metallogenic Belt. Econ. Geol. 118 (6), 1341–1370. https://doi.org/10.5382/econgeo.5009.

Dana, C.D.P., Lai, C.-K., Xia, X.-P., Geiger, M., 2024. Multiple mineralization events in the Central Borneo metallogenic belt, Indonesia: Insights from the Beruang Kanan orefield. Ore Geol. Rev. 169, 106087. https://doi.org/10.1016/j.oregeorev.2024.106087.

Davies, J.H.F.L., Sheldrake, T.E., Reimink, J.R., Wotzlaw, J.-F., Moeck, C., Finlay, A., 2018. Investigating complex isochron data using mixture models. Geochem. Geophys. Geosyst. 19 (10). https://doi.org/10.1029/2018GC007548.

Duuring, P., Hassan, L., Zelic, M., Gessner, K., 2016. Geochemical and spectral footprint of metamorphosed and deformed VMS-style mineralization in the Quinns district, Yilgarn Craton, Western Australia. Econ. Geol. 111, 1411–1438. https://doi.org/10.2113/econgeo.111.6.1411.

Eyles, N., Mory, A.J., Eyles, C.H., 2006. 50-Million-Year-Long Record of Glacial to Postglacial Marine Environments Preserved in a Carboniferous–Lower Permian Graben, Northern Perth Basin, Western Australia. J. Sediment. Res. 76 (3), 618–632. https://doi.org/10.2110/jsr.2006.047.

Gannoun, A., Tessalina, S., Bourdon, B., Orgeval, J.J., Birck, J.L., Allègre, C.J., 2003. Re–Os isotopic constraints on the genesis and evolution of the Dergamish and Ivanovka Cu (Co, Au) massive sulphide deposits, south urals, Russia. Chem. Geol. 196, 193–207. https://doi.org/10.1016/S0009-2541(02)00413-8.

Glorie, S., Simpson, A., Gilbert, S.E., Hand, M., Müller, A.B., 2024. Testing the reproducibility of in situ Lusingle bondHf dating using Lu-rich garnet from the Tørdal pegmatites, southern Norway. Chem. Geol. 653, 122038. https://doi.org/10.1016/j.chemgeo.2024.122038.

González-Jiménez, J.M., Griffin, W.L., Gervilla, F., Kerestedjian, T.N., O'Reilly, S.Y., Proenza, J.A., Pearson, N.J., Sergeeva, I., 2012. Metamorphism disturbs the Re–Os signatures of platinum-group minerals in ophiolite chromitites. Geology 40 (7), 659–662. https://doi.org/10.1130/G33064.1.

Goodfellow, W.D., McCutcheon, S.R., 2003. Geologic and genetic attributes of volcanic-hosted massive sulphide deposits of the Bathurst mining camp, northern New Brunswick. Econ. Geol. Monogr. 11, 245–311. https://doi.org/10.5382/Mono.11.13.

Goscombe, B.D., Blewett, R.S., Czarnota, K., Groenewald, B.A., Maas, R., 2009, Metamorphic evolution and integrated terrane analysis of the Eastern Yilgarn Craton: rationale, methods, outcomes and interpretation. Geoscience Australia, Record 2009/23.

Goscombe, B.D., Foster, D.A., Blewett, R., Czarnota, K., Wade, B., Groenewald, B.A., Gray, D., 2019. Neoarchaean metamorphic evolution of the Yilgarn Craton: a record of subduction, accretion, extension and lithospheric delamination. Precambr. Res. 335, 105441. https://doi.org/10.1016/j.precamres.2019.105441.

Guilliamse, J., 2014. Assessing the potential for volcanic-associated massive sulfide mineralization at Weld Range, using Golden Grove for comparison. Geological Survey of Western Australia, Report 141, 61p.

Groenewald, P.B., Doyle, M.G., Brown, S.J.A., Barnes, S.J., 2006, Stratigraphy and physical volcanology of the Archaean Kurnalpi Terrane, Yilgarn Craton – a field guide. GSWA Record 2006/11.

Hannah, J.L., Stein, H.J., 2013, Re–Os Isotope Geochemistry. In: Melezhik, V.A., Kump, L.R., Fallick, A.E., et al. (Eds.), Reading the Archive of Earth's Oxygenation, Volume 3: Global Events and the Fennoscandian Arctic Russia—Drilling Early Earth Project. Springer-Verlag, Berlin, Heidelberg, 1506-1513.

Hart, T.R., Gibson, H.L., Lesher, C.M., 2004. Trace element geochemistry and petrogenesis of felsic volcanic rocks associated with volcanogenic massive Cu–Zn–Pb sulfide deposits. Econ. Geol. 99 (5), 1003–1013. https://doi.org/10.2113/gsecongeo.99.5.1003.

Hassan, L.Y., 2014. The Yuinmery volcanogenic massive sulfide prospects: mineralization, metasomatism and geology. Geological Survey of Western Australia, Report 131, 65p.

Hawke, M.L., Meffre, S., Stein, H., Hilliard, P., Large, R., Gemmell, J.B., 2015. Geochronology of the DeGrussa volcanic-hosted massive sulphide deposit and associated mineralisation of the Yerrida, Bryah and Padbury Basins, Western Australia. Precambr. Res. 267, 250–284. https://doi.org/10.1016/j.precamres.2015.06.011.

Hayman, P.C., Hull, S.E., Cas, R.A.F., Summerhayes, E., Amelin, Y., Ivanic, T.J., Price, D., 2015. A new period of volcanogenic massive sulfide formation in the Yilgarn: a volcanological study of the ca 2.76 Ga Hollandaire VMS deposit, Yilgarn Craton, Western Australia. Aust. J. Earth Sci. 62 (2), 189–210. https://doi.org/10.1080/08120099.2015.1011399.

Hollis, S.P., Mole, D.R., Gillespie, P., Barnes, S.J., Tessalina, S., Cas, R.A.F., Hildrew, C., Pumphrey, A., Goodz, M.D., Caruso, S., Yeats, C.J., Verbeeten, A., Belford, S.M., Wyche, S., Martin, L.A.J., 2017a. 2.7 Ga plume associated VHMS mineralization in the Eastern Goldfields Superterrane, Yilgarn Craton: insights from the low temperature and shallow water, Ag-Zn-(Au) Nimbus deposit. Precambr. Res. 291, 119–142. https://doi.org/10.1016/j.precamres.2017.01.002.

Hollis, S.P., Podmore, D., James, M., Kneeshaw, A., Beaton, R., 2019a. Targeting VHMS mineralization at Erayinia in the Eastern Goldfields Superterrane using lithogeochemistry, soil chemistry and HyLogger data. J. Geochem. Explor. 207, 106379. https://doi.org/10.1016/j.gexplo.2019.106379.

Hollis, S.P., Podmore, D., James, M., Menuge, J.F., Doran, A.L., Yeats, C.J., Wyche, S., 2019b. VHMS mineralisation at Erayinia in the Eastern Goldfields Superterrane: geology and geochemistry of the metamorphosed King Zn deposit. Australian Journal of Earth Science 66, 153–181. https://doi.org/10.1080/08120099.2018.1515577.

Hollis, S.P., Wyche, S., Yeats, C.J., Barnes, S.J., Ivanic, T.J., Belford, S.M., Davidson, G.J., Roache, A.J., Wingate, M.T.D., 2015. A review of volcanic-hosted massive sulphide (VHMS) mineralization in the Archaean Yilgarn Craton, Western Australia: tectonic, stratigraphic and geochemical associations. Precambr. Res. 260, 113–135. https://doi.org/10.1016/j.precamres.2014.11.002.

Hollis, S.P., Yeats, C.J., Wyche, S., Barnes, S.J., 2017b. VHMS mineralization in the Yilgarn Craton, Western Australia: a review of known deposits and prospectivity analysis of felsic volcanic rocks. Geological Survey of Western Australia, Report 165, 68p.

Horstwood, M.S.A., Košler, J., Gehrels, G., Jackson, S.E., McLean, N.M., Paton, C., Pearson, N.J., Sircombe, K., Sylvester, P., Vermeesch, P., Bowring, J.F., Condon, D.J., Schoene, B., 2016. Community-derived standards for LA-ICP-MS U-(Th-)Pb geochronology: uncertainty propagation, age interpretation and data reporting. Geostand. Geoanal. Res. 40, 311–332. https://doi.org/10.1111/j.1751-908X.2016.00379.x.

Huston, D.L., Champion, D.C., Cassidy, K.F., 2014. Tectonic controls on the endowment of the Neoarchean Cratons in volcanic-hosted massive Sulfide deposits: evidence from Lead and Neodymium Isotopes. Econ. Geol. 109, 11–26. https://doi.org/10.2113/econgeo.109.1.11.

Huston, D.L., Pehrsson, S., Eglington, B.M., Zaw, K., 2010. The geology and metallogeny of volcanic-hosted massive sulfide deposits: variations through geologic time and with tectonic setting. Econ. Geol. 105, 571–591. https://doi.org/10.2113/gsecongeo.105.3.571.

IGO Ltd., 2017, Annual mineral resource and ore reserve statement, unpublished internal report, 71p.

Ivanic, T.J., Wingate, M.T.D., Kirkland, C.L., van Kranendonk, M.J., Wyche, S., 2010. Age and significance of voluminous mafic-ultramafic magmatic events in the Murchison Domain, Yilgarn Craton. Australian Journal of Earth Science 57, 597–614. https://doi.org/10.1080/08120099.2010.494765.

Jackson, S.E., Pearson, N.J., Griffin, W.L., Belousova, E.A., 2004. The application of laser ablation-inductively coupled plasma-mass spectrometry to in situ U–Pb zircon geochronology. Chem. Geol. 211, 47–69. https://doi.org/10.1016/j.chemgeo.2004.06.017.

Jones, S.A., 2024. 2730–2670 Ma rifting triggers sagduction prior to the onset of orogenesis at ca 2650 Ma: implications for gold mineralisation, Eastern Goldfields, Western Australia. Aust. J. Earth Sci. 71 (5), 647–672. https://doi.org/10.1080/08120099.2024.2337773.

Jones, S. A., 2007. Geology of the Erayinia 1:100 000 sheet. Perth, WA: Western Australia Geological Survey, 1:100 000 Geological Series Explanatory Notes, 37p.

Kelly, J., Hollis, S.P., Dana, C.D.P., Kneeshaw, A., Podmore, D., James, M., 2024. Characterization of a metamorphosed volcanic stratigraphy and VMS alteration halos using rock chip petrography and lithogeochemistry: a case study from king North, Yilgarn Craton, Western Australia. Minerals 14 (5). https://doi.org/10.3390/min14050481.

Kinny, P.D., Nutman, A.P., 1996. Zirconology of the Meeberrie gneiss, Yilgarn Craton, Western Australia: an early Archaean migmatite. Precambr. Res. 78, 165–178.

Kirkland, C.L., Abello, F., Danisik, M., Gardiner, N.J., Spencer, C., 2017. Mapping temporal and spatial patterns of zircon U–Pb disturbance: a Yilgarn Craton case study. Gondw. Res. 52, 39–47. https://doi.org/10.1016/j.gr.2017.08.004.

Kirkland, C.L., Spaggiari, C.V., Pawley, M.J., Wingate, M.T.D., Smithies, R.H., Howard, H.M., Tyler, I.M., Belousova, E.A., Poujol, M., 2011. On the edge: U–Pb, Lu–Hf, and Sm–Nd data suggests reworking of the Yilgarn craton margin during formation of the Albany-Fraser Orogen. Precambr. Res. 187 (3–4), 223–247. https://doi.org/10.1016/j.precamres.2011.03.002.

Kositcin, N., Brown, S.J.A., Barley, M.E., Krapež, B., Cassidy, K.F., Champion, D.C., 2008. SHRIMP U–Pb zircon age constraints on the late Archaean tectonostratigraphic architecture of the Eastern Goldfields Superterrane, Yilgarn Craton. Western Australia. Precambrian Research 161 (1–2), 5–33. https://doi.org/10.1016/j.precamres.2007.06.018.

Kramers, J.D., Tolstikhin, I.N., 1997. Two terrestrial lead isotope paradoxes, forward transport modelling, core formation and the history of the continental crust. Chem. Geol. 139, 75–110. https://doi.org/10.1016/S0009-2541(97)00027-2.

Krapež, B., Hand, J.L., 2008. Late Archaean deep-marine volcaniclastic sedimentation in an arc-related basin: the Kalgoorlie Sequence of the Eastern Goldfields Superterrane, Yilgarn Craton, Western Australia. Precambr. Res. 161, 89–113. https://doi.org/10.1016/j.precamres.2007.06.014.

Lane, K., 2011. Metamorphic and geochronological constraints on the evolution of the Kalinjala Shear Zone, Eyre Peninsula. University of Adelaide, Adelaide, Earth Sciences.

Lawley, C.J.M., Selby, D., 2012. Re–Os geochronology of quartz-enclosed ultrafine molybdenite: Implications for ore geochronology. Econ. Geol. 107, 1499–1505. https://doi.org/10.2113/econgeo.107.7.1499.

Lawley, C., Selby, D., Imber, J., 2013. Re–Os Molybdenite, Pyrite, and Chalcopyrite Geochronology, Lupa Goldfield, Southwestern Tanzania: Tracing Metallogenic Time Scales at Midcrustal Shear zones Hosting Orogenic Au deposits. Econ. Geol. 108 (7), 1591–1613. https://doi.org/10.2113/econgeo.108.7.1591.

Lehmann, B., Zhao, X., Zhou, M., Du, A., Mao, J., Zeng, P., Henjes-Kunst, F., Heppe, K., 2013. Mid-silurian back-arc spreading at the northeastern margin of Gondwana: the Dapingzhang dacite-hosted massive sulfide deposit, Lancangjiang zone, southwestern Yunnan, China. Gondwana Research 24 (2), 648–663. https://doi.org/10.1016/j.gr.2012.12.018.

Leybourne, M.I., Peter, J.M., Kidder, J.A., Layton-Mathews, D., Petrus, J.A., Rissman, C. F.W., Voinot, A., Bowell, R., Kyser, T.K., 2022. Stable and Radiogenic Isotopes in the Exploration for Volcanogenic Massive Sulfide Deposits. Can. Mineral. 60 (3), 4333–4468. https://doi.org/10.3749/canmin2000068.

Li, Y., Selby, D., Condon, D., Tapster, S., 2017. Cyclic Magmatic-Hydrothermal Evolution in Porphyry Systems: High-Precision U–Pb and Re–Os Geochronology Constraints on the Tibetan Qulong Porphyry Cu-Mo Deposit. Econ. Geol. 112, 1419–1440. https://doi.org/10.5382/econgeo.2017.4515.

Li, Y., Vermeesch, P., 2021. Short communication: Inverse isochron regression for Re–Os. K-Ca and Other Chronometers. Geochronology 3 (2), 415–420. https://doi.org/10.5194/gchron-3-415-2021.

Lijuan, Y., Chenghui, W., Juxing, T., Denghong, W., Wenjun, Q., Chao, L., 2014. Re–Os systematics of sulfides (chalcopyrite, bornite, pyrite and pyrrhotite) from the Jiama Cu–Mo deposit of Tibet, China. J. Asian Earth Sci. 79, 497–506. https://doi.org/10.1016/j.jseaes.2013.10.004.

Lobanov, K., Yakubchuk, A., Creaser, R.A., 2014. Besshi-type VMS deposits of the Rudny Altai (Central Asia). Econ. Geol. 109 (5), 1403–1430. https://doi.org/10.2113/econgeo.109.5.1403.

Maltese, A., Mezger, K., 2020. The Pb isotope evolution of Bulk Silicate Earth: Constraints from its accretion and early differentiation history. Geochim. Cosmochim. Acta 271, 179–193. https://doi.org/10.1016/j.gca.2019.12.021.

Marshall, B., Vokes, F.M., Larocque, A.C.L., 1998. Regional metamorphic remobilization: Upgrading and formation of ore deposits. Rev. Econ. Geol. 11, 19–38. https://doi.org/10.5382/Rev.11.02.

Masurel, Q., Thebaud, N., 2024. Deformation in the Agnew-Wiluna Greenstone Belt and host Kalgoorlie Terrane during the c. 2675–2630 ma Kalgoorlie Orogeny: 45 ma of horizontal shortening in a neoarchean back-arc region. Precambr. Res. 414, 107586. https://doi.org/10.1016/J.PRECAMRES.2024.107586.

Mathieson, L.M., Kirkland, C.L., Daggitt, M.L., 2025. Turning Trash into Treasure: Extracting Meaning from Discordant Data via a Dedicated Application. Geochem. Geophys. Geosyst. 26 (3). https://doi.org/10.1029/2024GC012066.

Mathur, R., Ruiz, J., Tornos, F., 1999. Age and sources of the ore at Tharsis and Rio Tinto, Iberian Pyrite Belt, from Re–Os isotopes. Miner. Deposita 34, 790–893. https://doi.org/10.1007/s001260050239.

Mazoz, A., Gonçalves, G.O., Lana, C., Buick, I.S., Corfu, F., Kamo, S.L., Wang, H., Yang, Y., Scholz, R., Queiroga, G., Fu, B., Martins, L., Schannor, M., De Abreu, A.T., Babinski, M., Peixoto, E., Ventura Santos, R., 2022. Khan River and Bear Lake: two Natural Titanite Reference Materials for High-Spatial Resolution U-Pb Microanalysis. Geostand. Geoanal. Res. 46, 701–733. https://doi.org/10.1111/ggr.12444.

McInnes, B.I.A., Keays, R.R., Lambert, D.D., Hellstrom, J., Allwood, J.S., 2008. Re–Os geochronology and isotope systematics of the Tanami, Tennant Creek and Olympic Dam Cu-Au deposits. Aust. J. Earth Sci. 55 (6–7), 967–981. https://doi.org/10.1080/08120090802097443.

Mikucki, E.J., Roberts, F.I., 2003, Metamorphic petrography of the Kalgoorlie region eastern goldfields granite-greenstone terrane METPET database. GSWA Record 2003/12.

McNaughton, N.J., Groves, D.I., 1996. A review of Pb-isotope constraints on the genesis of lode-gold deposits in the Yilgarn Craton, Western Australia. J. R. Soc. West. Aust. 79, 123–129.

Mole, D.R., Fiorentini, M.L., Cassidy, K.F., Thebaud, N., McCuaig, T.C., Doublier, M.P., Duuring, P., Romano, S.S., Maas, R., Belousova, E.A., Barnes, S.J., Miller, J., 2015. Crustal evolution, intra-cratonic architecture and the metallogeny of an Archaean craton. Geol. Soc. Lond. Spec. Publ. 393, 23–80. https://doi.org/10.1144/SP393.8.

Mole, D.R., Fiorentini, M.L., Thébaud, N., McCuaig, T.C., Cassidy, K.F., Kirkland, C.L., Wingate, M.T.D., Romano, S.S., Doublier, M.P., Belousova, E.A., 2012. Spatio-temporal constraints on lithospheric development in the southwest-central Yilgarn Craton, Western Australia. Aust. J. Earth Sci. 59 (5), 625–656. https://doi.org/10.1080/08120099.2012.691213.

Morelli, R.M., Creaser, R.A., 2007. Testing the robustness of Re–Os low level sulfide chronometers: an example from metamorphosed VMS ores, Trans Hudson orogen, Canada [abs.]. Geological Society of America Program with Abstracts 39, 276.

Morris, P.A., Riganti, A., Chen, S.F., 2007. Evaluating the provenance of Archean sedimentary rocks of the Diemals Formation (central Yilgarn Craton) using whole-rock chemistry and precise U–Pb zircon chronology. Aust. J. Earth Sci. 54 (8), 1123–1136.

Munhá, J., Relvas, J.M.R.S., Barriga, F.J.A.S., Conceição, P., Jorge, R.C.G.S., Mathur, R., Ruiz, J., Tassinari, C.C.G., 2005. Osmium isotope systematics in the Iberian Pyrite Belt. In: Mao, J., Bierlein, F. (Eds.), Mineral Deposit Research: Meeting the Global Challenge. Springer, Berlin, Heidelberg, pp. 663–666.

Nelson, D. R., 1995, 104973: Metadacite porphyry, east of Liberty Bore. In: Compilation of SHRIMP U–Pb zircon geochronology data, 1994. Perth, WA: Western Australia Geological Survey, Record 1995/3, 158-161.

Nelson, D.R., 1996, 1 121 77: foliated tonalite, Outcamp Bore. in Compilation of SHRIMP U–Pb zircon geochronology data, 1995: Western Australia Geological Survey, Record 1996/5, p. 71–74.

Nelson, D.R., 1997. Evolution of the Archaean granite-greenstone terranes of the Eastern Goldfields, Western Australia: SHRIMP U–Pb zircon constraints. Precambr. Res. 83 (1–3), 57–81. https://doi.org/10.1016/S0301-9268(97)00005-3.

Nieuwland, D.A., Compston, W., 1981. Crustal evolution in the Yilgarn Block near Perth, Western Australia. Geological Society of Australia Special Publication 7, 159–171.

Norman, M.D., 2023. The 187Re-187Os and 190Pt-186Os Radiogenic Isotope Systems: Techniques and applications to Metallogenic Systems. In: Huston, D., Gutzmer, J. (Eds.), Isotopes in Economic Geology, Metallogenesis and Exploration. Mineral Resource Reviews. Springer, Cham. https://doi.org/10.1007/978-3-031-27897-6_4.

Norris, A., Danyushevsky, L., 2018. Towards estimating the complete uncertainty budget of quantified results measured by LA-ICP-MS. Goldschmidt, Boston.

Nozaki, T., Kato, Y., Suzuki, K., 2010. Re–Os geochronology of the Iimori Besshi-type massive sulfide deposit in the Sanbagawa metamorphic belt. Japan. Geochimica et Cosmochimica Acta 74 (15), 4322–4331. https://doi.org/10.1016/j.gca.2010.04.05.

Nozaki, T., Kato, Y., Suzuki, K., 2013. Late Jurassic ocean anoxic event: evidence from voluminous sulphide deposition and preservation in the Panthalassa. Sci. Rep. 3, 1889. https://doi.org/10.1038/srep01889.

Nozaki, T., Suzuki, K., Ravizza, G., Kimura, J.-I., Chang, Q., 2012. A Method for rapid determination of Re and Os isotope compositions using ID-MC-ICP-MS combined with the sparging method. Geostand. Geoanalytical Res. 36, 131–148. https://doi.org/10.1111/j.1751-908X.2011.00125.x.

Ohta, J., Nozaki, T., Sato, H., Ashida, K., Kato, Y., 2022. Precise and accurate analytical method for determination of osmium isotope ratios at the 1–15 pg level by MC-ICP-MS equipped with sparging introduction and high-sensitivity discrete dynode-type ion-counting detectors. J. Anal. At. Spectrom 37, 1600–1610. https://doi.org/10.1039/D2JA00089J.

Pawley, M.J., Wingate, M.T.D., Kirkland, C.L., Wyche, S., Hall, C.E., Romano, S.S., Doublier, M.P., 2012. Adding pieces to the puzzle: episodic crustal growth and a new terrane in the northeast Yilgarn Craton, Western Australia. Aust. J. Earth Sci. 59 (5), 603–623. https://doi.org/10.1080/08120099.2012.696555.

Paton, C., Hellstrom, J., Paul, B., Woodhead, J., Hergt, J., 2011. Iolite: Freeware for the visualisation and processing of mass spectrometric data. J. Anal. At. Spectrom 26, 2508–2518. https://doi.org/10.1039/c1ja10172b.

Peucker-Ehrenbrink, B., Jahn, B., 2001. Rhenium-osmium isotope systematics and platinum group element concentrations: Loess and the upper continental crust. Geochem. Geophys. Geosyst. 2, 1–22. https://doi.org/10.1029/2001GC000172.

Petrus, J.A., Kamber, B.S., 2012. VizualAge: a novel approach to laser ablation ICP-MS U-Pb geochronology data reduction. Geostand. Geoanal. Res. 36, 247–270. https://doi.org/10.1111/j.1751-908X.2012.00158.x.

Piercey, S.J., 2011. The setting, style, and role of magmatism in the formation of volcanogenic massive sulfide deposits. Miner. Deposita 46, 449–471. https://doi.org/10.1007/s00126-011-0341-z.

Plimer, I.R., 1987. Remobilization in high-grade metamorphic environments. Ore Geol. Rev. 2 (1–3), 231–245. https://doi.org/10.1016/0169-1368(87)90030-8.

Rooney, A.D., Hnatyshin, D., Toma, J., Saintilan, N.J., Millikin, A.E.G., Selby, D., Creaser, R.A., 2024. Application of the ^{187}Re-^{187}Os geochronometer to crustal materials: Systematics, methodology, data reporting, and interpretation. GSA Bull. 136 (9), 4091–4129. https://doi.org/10.1130/B37294.1.

Saintilan, N.J., Sheldrake, T.E., Creaser, R.A., Selby, D., Zieg, J., Boyce, A., Chelle-Michou, C., 2021. Synsedimentary to diagenetic Cu±Co mineralization in Mesoproterozoic pyritic shale driven by magmatic-hydrothermal activity on the edge of the Great Falls Tectonic Zone-Black Butte, Helena Embayment, Belt-Purcell Basin, USA: evidence from sulfide Re–Os isotope geochemistry. Lithosphere 2021 (1). https://doi.org/10.2113/2021/7866186.

Schreefel, R., Fisher, C.M., Kemp, I.S., Hagemann, S.G., Masurel, Q., Th́ ebaud, N., Davy's, C., Martin, L., Lowrey, J.R., Lu, Y., Cassidy, K.F., 2024, Crustal Growth in the Archean: Insights from Zircon Petrochronology of the Far-East Yilgarn Craton. Precambrian Research, 107253. DOI: 10.1016/J.PRECAMRES.2023.107253.

Schulz, T., Viehmann, S., Hezel, D.C., Koeberl, C., Bau, M., 2021. Highly Siderophile elements and coupled Fe-Os Isotope Signatures in the Temagami Iron Formation, Canada: possible Signatures of Neoarchean Seawater Chemistry and Earth's Oxygenation history. Astrobiology 21 (8), 924–939. https://doi.org/10.1089/ast.2020.2311.

Selby, D., Kelley, K.D., Hitzman, M.W., Zieg, J., 2009. Re–Os sulfide (bornite, chalcopyrite, and pyrite) systematics of the carbonate-hosted copper deposits at Ruby Creek, Southern Brooks Range. Alaska. Economic Geology 104 (3), 437–444. https://doi.org/10.2113/gsecongeo.104.3.437.

Sharpe, R., Gemmell, J.B., 2002. The Archean Cu–Zn magnetite-rich Gossan Hill volcanic-hosted massive sulfide deposit, Western Australia: genesis of a multistage hydrothermal system. Econ. Geol. 97 (3), 517–539. https://doi.org/10.2113/gsecongeo.97.3.517.

Simpson, A., Gilbert, S., Tamblyn, R., Hand, M., Spandler, C., Gillespie, J., Nixon, A., Glorie, S., 2021. In-situ Lu Hf geochronology of garnet, apatite and xenotime by LA ICP MS/MS. Chem. Geol. 577, 120299. https://doi.org/10.1016/j.chemgeo.2021.120299.

Simpson, A., Glorie, S., Hand, M., Spandler, C., Gilbert, S., 2023. Garnet Lu–Hf speed dating: a novel method to rapidly resolve polymetamorphic histories. Gondw. Res. 121, 215–234. https://doi.org/10.1016/j.gr.2023.04.011.

Smithies, R.H., Gessner, K., Lu, Y., Kirkland, C.L., Ivanic, T., Lowrey, J.R., Champion, D. C., Sapkota, J., Masurel, Q., Quentin de Gromard, R., 2023. Geochemical mapping of lithospheric architecture disproves Archean terrane accretion in the Yilgarn craton. Geology 52, 141–146. https://doi.org/10.1130/G51707.1.

Smoliar, M.I., Walker, R.J., Morgan, J.W., 1996. Re–Os ages of group IIA, IIIA, IVA, and IVB iron meteorites. Science 271, 1099–1102. https://doi.org/10.1126/science.271.5252.1099.

Sláma, J., Košler, J., Condon, D.J., Crowley, J.L., Gerdes, A., Hanchar, J.M., Horstwood, M.S.A., Morris, G.A., Nasdala, L., Norberg, N., Schaltegger, U., Schoene, B., Tubrett, M.N., Whitehouse, M.J., 2008. Plešovice zircon — a new natural reference material for U–Pb and Hf isotopic microanalysis. Chem. Geol. 249, 1–35. https://doi.org/10.1016/j.chemgeo.2007.11.005.

Spandler, C., Hammerli, J., Sha, P., Hilbert-Wolf, H., Hu, Y., Roberts, E., Schmitz, M., 2016. MKED1: a new titanite standard for in situ analysis of Sm-Nd isotopes and U–Pb geochronology. Chem. Geol. 425, 110–126. https://doi.org/10.1016/j.chemgeo.2016.01.002.

Stein, H.J., Markey, R.J., Morgan, J.W., Selby, D., Creaser, R.A., McCuaig, T.C., Behn, M., 2001. 2001, Re–Os dating of Boddington molybdenites, SW Yilgarn: two Au mineralization events. AGSO-Geoscience Australia, Record 37, 469–471.

Stein, H.J., Morgan, J.W., Markey, R.J., Williams-Jones, A.E., Heiligmann, M., Clark, J. R., 1999. Re–Os age for the Hemlo Au deposit, Ontario, Canada: durability of the Re–Os chronometer. Eos Trans. AGU 80, F1082.

Stein, H.J., Morgan, J.W., Schersten, A., 2000. Re–Os dating of low-level highly radiogenic (LLHR) sulfides: the Harnäs gold deposit, southwest Sweden, records continental-scale tectonic events. Econ. Geol. 95, 1657–1671. https://doi.org/10.2113/gsecongeo.95.8.1657.

Stein, H., Sundblad, K., Markey, R.J., Morgan, J.W., Motuza, G., 1998. Re–Os ages for Archean molybdenite and pyrite, Kuittila-Kivisuo, Finland and Proterozoic molybdenite, Kabeliai, Lithuania: testing the chronometer in a metamorphic and metasomatic setting. Miner. Deposita 33, 329–345. https://doi.org/10.1007/s001260050153.

Stein, H., Hannah, J., 2015, Rhenium–Osmium Geochronology: Sulfides, Shales, Oils, and Mantle. In: Rink, W.J., Thompson, J.W. (eds) Encyclopedia of Scientific Dating Methods. Encyclopedia of Earth Sciences Series. Springer, Dordrecht. DOI: 10.1007/978-94-007-6304-3_36.

Stern, R.A., Bodorkos, S., Kamo, S.L., Hickman, A.H., Corfu, F., 2009. Measurement of SIMS Instrumental Mass Fractionation of Pb Isotopes during Zircon Dating. Geostand. Geoanal. Res. 33, 145–168. https://doi.org/10.1111/j.1751-908X.2009.00023.x.

Swager, C.P., 1995. Geology of the greenstone terranes in the Kurnalpi-Edjudina region, southeastern Yilgarn Craton. Western Australia Geological Survey Report 47, 31.

Swager, C.P., 1997. Tectono-stratigraphy of the late Archaean greenstone terranes in the southern Eastern Goldfields, Western Australia. Precambr. Res. 83, 11–42. https://doi.org/10.1016/S0301-9268(97)00003-X.

Terakado, Y., 2001. Re–Os dating of the Kuroko ore deposits from the Hokuroku district, Akita Prefecture, Northeast Japan. J. Geol. Soc. Jpn. 107, 354–357.

Tessalina, S.G., Bourdon, B., Maslennikov, V.V., Orgeval, J.-J., Birck, J.-L., Gannoun, A., Capmas, F., Allègre, C.-J., 2008. Osmium isotope distribution within the Palaeozoic Alexandrinka seafloor hydrothermal system in the Southern urals, Russia. Ore Geol. Rev. 33, 70–80. https://doi.org/10.1016/j.oregeorev.2005.05.003.

Tessalina, S.G., Jourdan, F., Belogub, E.V., 2017. Significance of late Devonian-lower Carboniferous ages of hydrothermal sulphides and sericites from the urals Volcanic-Hosted Massive Sulphide deposits. Ore Geol. Rev. 85, 131–139. https://doi.org/10.1016/j.oregeorev.2016.08.005.

Thirlwall, M.F., 2002. Multicollector ICP-MS analysis of Pb isotopes using a 207Pb-204Pb double spike demonstrates up to 400 ppm/amu systematic errors in Tl-normalization. Chem. Geol. 184 (3–4), 255–279. https://doi.org/10.1016/S0009-2541(01)00365-.

Thorpe, R.I., Hickman, A.H., Davis, D.W., Mortensen, J.K., Trendall, A.F., 1992. U–Pb zircon geochronology of Archaean felsic units in the Marble Bar region, Pilbara Craton. Western Australia. Precambrian Research 56 (3–4), 169–189. https://doi.org/10.1016/0301-9268(92)90100-3.

Tomkins, A.G., Pattison, D.R.M., Frost, B.R., 2007. On the initiation of metamorphic sulfide anatexis. J. Petrol. 48 (3), 511–535. https://doi.org/10.1093/petrology/egl070.

Toulmin III, P., Barton Jr., P.B., 1964. A thermodynamic study of pyrite and pyrrhotite. Geochim. Cosmochim. Acta 28 (5), 641–671. https://doi.org/10.1016/0016-7037(64)90083-3.

Van Kranendonk, M.J., Ivanic, T.J., Wingate, M.T.D., Kirkland, C.L., Wyche, S., 2013. Long-lived, autochthonous development of the Archean Murchison Domain, and implications for Yilgarn Craton tectonics. Precambr. Res. 229, 49–92. https://doi.org/10.1016/j.precamres.2012.08.009.

Veevers, J.J., Saeed, A., Belousova, E.A., Griffin, W.L., 2005. U–Pb ages and source composition by Hf-isotope and trace-element analysis of detrital zircons in Permian sandstone and modern sand from southwestern Australia and a review of the paleogeographical and denudational history of the Yilgarn Craton. Earth Sci. Rev. 68 (3–4), 245–279. https://doi.org/10.1016/j.earscirev.2004.05.005.

Vermeesch, P., 2018. IsoplotR: a free and open toolbox for geochronology. Geosci. Front. 9, 1479–1493. https://doi.org/10.1016/j.gsf.2018.04.001.

Viehmann, S., Bau, M., Hoffmann, J.E., et al., 2015. Geochemistry of the Krivoy Rog Banded Iron Formation, Ukraine, and the impact of peak episodes of increased global magmatic activity on the trace element composition of Precambrian seawater. Precambr. Res. 270, 165–180. https://doi.org/10.1016/j.precamres.2015.09.015.

Walker, R.J., Nisbet, E., 2002. 187Os isotopic constraints on Archean mantle dynamics. Geochim. Cosmochim. Acta 66 (18), 3317–3325. https://doi.org/10.1016/S0016-7037(02)00932-8.

Wang, J.-Y., Santosh, M., Yang, C.-X., Nakagawa, M., 2021. Revisiting the type area VMS deposit of Besshi, SW Japan: In-situ trace element chemistry, isotopes and Re–Os age of sulfides. Ore Geol. Rev. 130, 103955. https://doi.org/10.1016/j.oregeorev.2020.103955.

Wiedenbeck, M., Allé, P., Corfu, F., Griffin, W.L., Meier, M., Oberli, F., Quadt, A.V., Roddick, J.C., Spiegel, W., 1995. Three natural zircon standards for U-Th-Pb, Lu–Hf, trace element and REE analyses. Geostand. Geoanal. Res. 19, 1–23. https://doi.org/10.1111/j.1751-908X.1995.tb00147.x.

Wilde, S.A., Spaggiari, C.V., 2007, The Narryer Terrane, Western Australia: a review. In: Van Kranendonk, M.J., Smithies, R.H., Bennett, V.C. (Eds.), Earth's oldest rocks, developments in Precambrian geology, vol 15. Elsevier, Amsterdam, 275–304. DOI: 10.1016/S0166-2635(07)15036-2.

Wingate, M.T.D., Bodorkos, S., 2007a, 177919: felsic metavolcanic rock, Urania Prospect; Geochronology Record 666. Geological Survey of Western Australia, 4p.

Wingate, M.T.D., Bodorkos, S., 2007b, 177933: hornblende granodiorite, Camel Bore; Geochronology Record 675. Geological Survey of Western Australia, 4p.

Wingate, M.T.D., Lu, Y., Kirkland, C.L., Spaggiari, C.V., 2016. 182419: Granite gneiss, Coonana Hill, Geochronology Record 1300. Geological Survey of Western Australia, Perth WA, p. 4p.

Wingate, M.T.D., Morris, P.A., Pirajno, F., Pidgeon, R.T., 2005. Two Large Igneous Provinces in Late MesoProterozoic Australia vol. 81, 151.

Witt, W.K., Cassidy, K.F., Lu, Y.-J., Hagemann, S.G., 2020. The tectonic setting and evolution of the 2.7 Ga Kalgoorlie–Kurnalpi Rift, a world-class Archean gold province. Miner. Deposita 55, 601–631. https://doi.org/10.1007/s00126-017-0778-9.

Wyche, S., Pawley, M.J., Chen, S.F., Ivanic, T.J., Zibra, I., Van Kranendonk, M.J., Spaggiari, C.V., Wingate, M.T.D., 2014, Geology of the northern Yilgarn Craton, in Youanmi and southern Carnarvon seismic and magnetotelluric (MT) workshop compiled by S. Wyche, T.J. Ivanic and I. Zibra. Geological Survey of Western Australia, Record 2013/6, 31–60.

Xu, J., Hart, C.J.R., Wang, L., Chu, H., Lin, L., Wei, X., 2011. Carbonic fluid overprints in volcanogenic massive sulfide deposits: examples from the Kelan volcanosedimentary basin, Altaides, China. Economic Geology 106 (1), 145–155. https://doi.org/10.2113/econgeo.106.1.145.

Yeats, C.J., Groves, D.I., 1998. The Archaean Mount Gibson gold deposits, Yilgarn Craton, Western Australia: Products of combined synvolcanic and syntectonic alteration and mineralisation. Ore Geol. Rev. 113, 103–129. https://doi.org/10.1016/S0169-1368(97)00015-2.

Zametzer, A., Kirkland, C.L., Barham, M., Smithies, R.H., Huston, D.L., Champion, D.C., 2023. Archean Pb isotope variability tracks crust-mantle fractionation, granite production, and ore deposit formation. Chem. Geol. 620, 121327. https://doi.org/10.1016/j.chemgeo.2023.121327.

Zametzer, A., Kirkland, C.L., Hartnady, M.I.H., Barham, M., Champion, D.C., Bodorkos, S., Smithies, R.H., Johnson, S.P., 2022. Applications of Pb isotopes in granite K-feldspar and Pb evolution in the Yilgarn Craton. Geochim. Cosmochim. Acta 320, 279–303. https://doi.org/10.1016/j.gca.2021.11.029.

Zeng, Z., Chen, S., Selby, D., Yin, D., Yin, X., Wang, X., 2014. Rhenium–osmium abundance and isotopic compositions of massive sulfides from modern deep-sea hydrothermal systems: Implications for vent associated ore forming processes. Earth Planet. Sci. Lett. 396, 223–234. https://doi.org/10.1016/j.epsl.2014.04.017.

Zhimin, Z., Yali, S., 2013. Direct Re–Os dating of chalcopyrite from the Lala IOCG deposit in the Kangdian Copper Belt, China. Economic Geology 108 (4), 871–882. https://doi.org/10.2113/econgeo.108.4.871.